THERMO-MECHANICAL MODELING AND MICROSTRUCTURAL EVOLUTION OF A CAST ALUMINUM ALLOY

BY

TRACY JAYNE SMITH

B.S., University of Connecticut, 1996

THESIS

Submitted in partial fulfillment of the requirements
for the degree of Master of Science in Mechanical Engineering
in the Graduate College of the
University of Illinois at Urbana-Champaign, 1998

Urbana, Illinois

ABSTRACT

A modified two state variable unified constitutive model is presented to model the high temperature stress-strain behavior of a 319 cast aluminum alloy with a T7 heat treatment. A systematic method is outlined with which to determine the material parameters used in the experimentally based model. The microstructural processes affecting the material behavior were identified using TEM microscopy and consequently correlated with the model parameters. The stress-strain behavior was found to be dominated by the decomposition of the metastable θ' precipitates within the dendrites and subsequent coarsening of the θ phase which is manifested through remarkable softening with cycling and time. Pronounced dimensional instabilities were observed to occur rapidly if the material was exposed to 300°C. The model was found to accurately simulate experimental stress-strain behavior such as strain rate sensitivity, cyclic softening, aging effects, transient material behavior, and stress relaxation in addition to capturing the main deformation mechanisms and microstructural changes as a function of temperature and inelastic strain rate.

ACKNOWLEDGMENTS

The research was supported by Ford Motor Company, Dearborn, MI. All scanning and transmission electron microscopy work was performed in the Center for Microanalysis of Materials, University of Illinois at Urbana-Champaign, which is supported by the US Department of Energy under grant DEFG02-91-ER45439.

I would like to gratefully acknowledge my advisor, Professor Huseyin Sehitoglu, for his guidance and advice. As well as for allowing me some excellent opportunities and experiences during my work towards my Master of Science. In addition, I want to express my appreciation to Dr. Hans Maier for performing the SEM and TEM microscopy work, along with engaging in some extremely insightful discussions.

I especially thank Bob for his love, friendship, support, and encouragement, and without whom the past year and a half would not have been so fulfilling. Finally, I wish to dedicate this work to my parents and thank them for their endless support and encouragement.

TABLE OF CONTENTS

LIST OF TABLES

LIST OF FIGURES

NOMENCLATURE

a_1, a_2, a_3	Back stress hardening term material parameters
A	Flow rule material constant
A_1', A_2', A_3'	Back stress hardening term material parameters
B	Drag stress hardening term material constant
B_3	Drag stress recovery term material parameter
B_3', B_3''	Drag stress recovery term material constants
c	Back stress recovery temperature dependent material parameter
c', d, e	Back stress recovery material constants
h_α	Back stress hardening term
h_k	Drag stress hardening term
ΔH	Activation energy
K	Drag stress
K^*	Recovered value of drag stress at room temperature
$\dot{K}$	Drag stress rate
K_{rec}	Fully recovered drag stress at a given temperature
K_{sat}	Saturated drag stress
n_1	Power law creep exponent
n_2	Plasticity exponent
r_α^D	Dynamic recovery term
r_α^S	Static recovery term
r_k	Drag stress recovery term
R	Gas constant
S_{ij}	Deviatoric stress

S_{ij}^{c}	Deviatoric back stress
T	Temperature
$\dot{T}$	Temperature rate
$\bar{\alpha}$	Effective back stress
$\dot{\varepsilon}_{ij}^{in}$	Inelastic strain rate
$\dot{\bar{\varepsilon}}_{ij}^{in}$	Effective inelastic strain rate
Θ	Drag stress temperature dependence term
$\bar{\sigma}$	Effective stress

1. INTRODUCTION

The purpose of this study is to present a constitutive model which is capable of modeling the stress-strain behavior of cast aluminum alloys at high temperature. Such a model needs to accurately predict material responses such as, hardening and recovery behavior during plastic deformation, cyclic hardening and softening to a saturated response, strain rate sensitivity at high temperatures, stress relaxation as a result of strain holds, creep behavior at high temperature during stress holds, and thermo-mechanical behavior in response to simultaneous cycling of temperature and strain. An accurate, reliable and stable model is imperative for capturing the effects of the considerable microstructural changes that occur in the cast aluminum alloys during extended high temperature exposure. Well selected experiments which expose the material's behavior under various loading and temperature histories are an essential requirement for an accurate model.

A previously developed, experimentally based, unified constitutive model[1] was modified in order to model the stress-strain response of the cast aluminum alloy. The material constants used in the constitutive equations were established from experiments, and the microstructural processes dominating the material deformation behavior were correlated with the model. In order to comprehend a material's behavior it is imperative to correlate the mechanical behavior with the microstructure and with the inherent microstructural changes which occur during plastic deformation and extended thermal exposure at high temperatures.

The accuracy of the model can be verified through comparisons of experimental results with those results obtained from the model. The first phase in verifying the model was established by comparing experimental data used in developing the model with their respective simulations. These results are covered in Chapter 4. The second step in verifying the accuracy and reliability of the model was to study the predictive capabilities of the model through complex loading histories and subsequent experiments which were not utilized in determining the material parameters, such as thermo-mechanical fatigue tests, low stress-high temperature creep tests, and isothermal fatigue tests with dwell periods. Thermo-mechanical fatigue tests were employed to study the transient material behavior whereas isothermal fatigue tests with dwell periods in compression and tension yielded information on the stress relaxation behavior of the material.

The predictive capabilities of the model are extremely important when applying the model to predict the material's mechanical behavior in practical applications. For example, engine operation involves transients during both engine start-up and shut-down, in addition to periods of high temperature exposure during steady-state operation. This work also demonstrates that accurate modeling of a component's deformation behavior requires well defined and well controlled process conditions during casting since variability in the microstructure significantly affects the material's stress-strain response.

2. BACKGROUND

Improvements in engine performance have caused the temperatures in aluminum cylinder heads to increase from below 170°C in earlier engines[2] to peak temperatures well above 200°C[3,4] in recent engines. This and the increased competition in the automotive industry has triggered considerable effort directed towards improving cast aluminum alloys. The majority of studies have placed emphasis on comprehending various microstructural effects, such as porosity, intermetallic morphology, and secondary dendrite arm spacing, on the mechanical properties.

Microstructural effects are most easily quantified by varying the solidification rate of the casting and the subsequent aging treatment. Varied cooling rates introduce microstructural differences such as secondary dendrite arm spacing (SDAS) and porosity[5,6]. Vorren et al.[6] observed that increased solidification rate resulted in enhanced mechanical properties such as ultimate strength, ductility, fracture toughness, and fatigue resistance. The effects of porosity, intermetallics, and silicon modification are well established and have been shown to mainly decrease the ductility of cast aluminum alloys at ambient temperatures[5,7-9]. Wickberg et al.[5] studied the effects of cooling rate, porosity, and intermetallics on the fatigue life of a cast aluminum alloy. They found that the fatigue life decreased with increasing secondary dendrite arm spacing, increasing pore size, and increasing volume fraction of both porosity and intermetallics. Boileau and Allison[7], and Beumler[9] found that modifying the silicon phase through the addition of strontium did not result in a statistically significant change in fatigue life or a change in tensile strength. However, Gundlach et al.[8] did conclude that the thermal fatigue life of 319 and 356 alloys was dependent upon the morphology of the iron rich intermetallic phase.

The performance of these cast aluminum alloys have also been improved by modeling the casting[10] and subsequent thermal processing[11]. In addition, the aging treatment of these alloys imparts precipitates that enhance strength and alter fatigue and fracture performance. Vijayaraghavan et al.[10] used a micro-model approach to model the solidification. This approach can be considered as semi-empirical since experimental results were used to estimate the nucleation and growth kinetics. Shercliff and Ashby[11] formulated a model that described the changes in yield strength due to age hardening. The model was developed using the fundamental principles of phase equilibrium, precipitate coarsening and dislocation-precipitate interactions. The approach proved successful for binary aluminum alloys but encountered problems when modeling the aging curves of more complex aluminum alloys.

Although studies have been performed on characterizing, modifying and developing aluminum casting alloys[12,13], studies on the mechanical behavior of these alloys under high temperature conditions such as encountered in the service conditions of modern cylinder heads are still rare. To date, work has been performed to study and to model the thermal fatigue life of these alloys under thermal cycling between ambient and cylinder head service temperature[8,14-16]. Jonason[15] studied the thermal fatigue of actual cylinder heads by internally heating the cylinder head via induction coils in the inlet and exhaust valves, and cooling to the minimum temperature was achieved by running cooling water through the inside of the cylinder head. This study concluded that an alloy with good thermal fatigue resistance should have a low Si content, low porosity level, low levels of Fe, Zn and Ni, and a sufficient level of Cu to ensure strength at elevated temperatures without reducing ductility. Velasco et al.[16] attempted to model the fatigue behavior of an aluminum alloy by utilizing simple expressions for the strain hardening and relaxation behavior of the material. In addition, he compared the fatigue life with a simple empirical expression without much success. Additional research has focused on the wear resistance[12,17] of cast aluminum alloys used in engine blocks, and mechanical testing and characterization work of cast aluminum alloys used in engine components[18] and diesel cylinder heads[4].

3. MATERIAL AND EXPERIMENTAL PROCEDURES

3.1 Material and Sample Preparation

A cast aluminum 319 alloy with a T7 heat treatment, with composition shown in Table 1, was used in the present study. The T7 heat treatment is comprised of an 8h. solutionizing treatment at 495°C, followed by a boiling water quench and a 4h. aging treatment. This heat treatment produces an overaged microstructure which is intended to improve dimensional stability. In general, the overaged microstructure does not exhibit dimensional changes under high temperature exposure. However, section 6.3 and Chapter 7 discuss the effects of observed dimensional changes on the alloy's creep behavior at low stresses (<40MPa) and high temperature (300°C).

Table 1

Chemical composition of Al 319

wt%	Si	Cu	Mg	Mn	Fe	Ti	Zn	Cr	Al
min.	7.2	3.3	0.25	0.20	-	-	-	-	balance
max.	7.7	3.7	0.35	0.30	0.40	0.25	0.25	0.05	balance

The samples for tensile, fatigue and creep testing were prepared from a sand-cast wedge with a copper chill positioned at the apex of the wedge. The wedge geometry results in different solidification rates based upon a similar principle as the varied cooling rate castings used in earlier work[5,6]. This solidification control permits the machining of samples with controlled secondary dendrite arm spacing (SDAS). A sketch of the wedge geometry and relative positions of different SDAS is shown in Figure 1. All samples were tested with a polished surface finish and depending upon the type of test the diameter of the gage section ranged from 5.0-7.6mm. Figure 2 displays a sketch of the specimen, with corresponding dimensions, which was used for the thermo-mechanical and the low-stress, high-temperature experiments. Samples were studied with a SDAS ranging from 20-100μm. However, all data reported in this work is for a range of SDAS between 50-60μm.

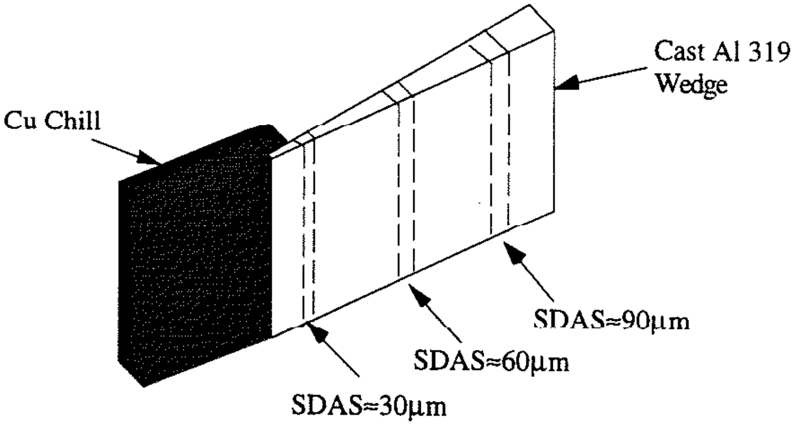

note: not to scale

Figure 1: Schematic of a wedge-shaped sand casting.

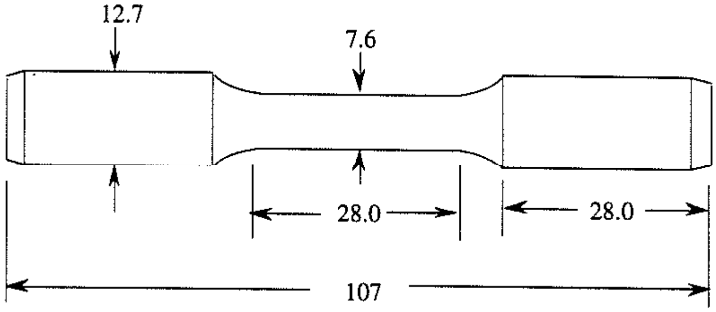

*all dimensions are in mm.
note: not to scale

Figure 2: Schematic of sample and dimensions.

3.2 Experimental Procedure

3.2.1 Mechanical Testing

Tests performed at the University of Illinois were combined with data provided by Ford Motor Company's Scientific Research Laboratory. The thermo-mechanical fatigue tests and low stress high temperature experiments were performed in the High Temperature Materials Laboratory at the University of Illinois using a servo-hydraulic Instron test machine in conjunction with a 15kW induction heater.

In all cases, creep experiments were conducted at constant load and a temperature of either 150°C or 250°C. Isothermal fatigue tests in the low-cycle fatigue regime were conducted under closed-loop, full reversed total strain control using a triangular waveshape. Tests were performed over a temperature range from 20-250°C and strain rates from $5\mathrm{x}10^{-5}\mathrm{s}^{-1}$ to $5\mathrm{x}10^{-3}\mathrm{s}^{-1}$. The monotonic tensile tests covered the same temperature range (20°C-250°C) as the isothermal fatigue tests. The strain rate was again $5\mathrm{x}10^{-5}\mathrm{s}^{-1}$ with the exception of the room temperature tensile tests which were conducted at a strain rate of $5\mathrm{x}10^{-2}\mathrm{s}^{-1}$.

The thermo-mechanical fatigue tests were conducted in total strain control under out-of-phase (OP) conditions in which the maximum mechanical strain coincides with the minimum temperature. The strain and temperature waveforms followed a triangular waveshape, as shown in Figure 3. The tests were performed at a strain rate of $5\mathrm{x}10^{5-}\mathrm{s}^{-1}$ over a temperature range of 100-300°C and a strain range of 0.6%.

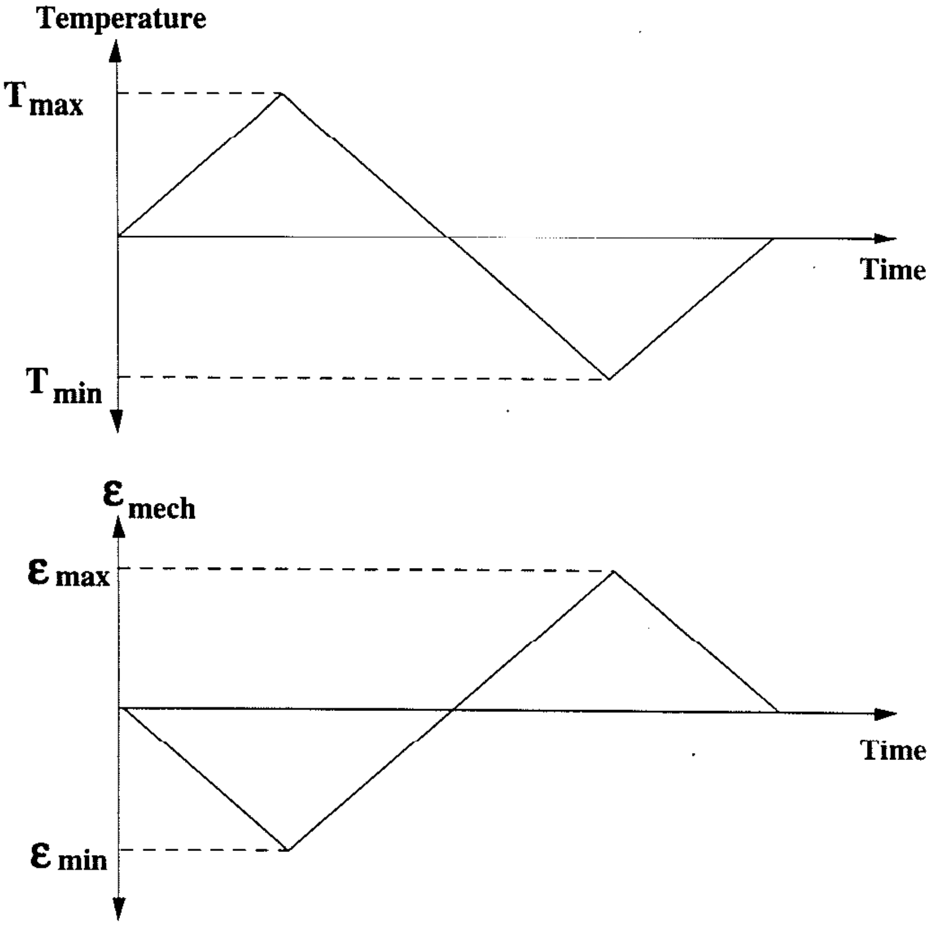

Figure 3: Thermo-mechanical fatigue waveforms for temperature and mechanical strain for an out-of-phase experiment.

The isothermal fatigue dwell tests were also conducted under strain control at a strain rate of $5\times10^{-5}s^{-1}$, a temperature of 250°C, and a strain range of 0.5%. Tests were implemented with a two minute dwell at the maximum tensile strain or at the maximum compressive strain. Failure for both the thermo-mechanical fatigue and isothermal fatigue dwell tests was considered to be the cycle at which the maximum tensile load had decreased to 50% of the average maximum tensile load observed in the 2nd and 3rd cycles. The low stress, high temperature experiments were conducted under load control at a temperature of 300°C for a duration of 100h. The experiment at 40MPa being the exception in which the sample failed before reaching the 100h. point.

3.2.2 Microscopy

The effects of cyclic deformation and long-term high-temperature exposure on the evolution of the microstructure were studied by transmission electron microscopy (TEM). For TEM work, slices were sectioned from samples normal to the external stress axis and then ground carefully to a thickness of 150 μm. Final thinning to electron transparency was accomplished by dimple-grinding to a foil thickness of 20 μm followed by ion-milling. To minimize ion beam damage to the sample, the sample holder was cooled with liquid nitrogen.

The microstructure was studied using a Philips CM12 microscope operated at a nominal accelerating voltage of 120 kV. Scanning electron microscopy was used to evaluate the size and distribution of voids and intermetallics which govern crack nucleation, crack growth and ductility. Voids and intermetallics were found to form preferentially in the interdendritic regions. On the contrary, stress-strain behavior is governed mostly by the microstructure within the dendrites. SEM and optical microscopy were used to ensure that the electron transparent area studied in TEM was located within a dendrite, since TEM analysis indicated that the size and distribution of precipitates changed considerably when approaching the interdendritic regions. Larger θ (Al_2Cu) precipitates were also observed at grain boundaries and silicon/matrix interfaces. These precipitates will not be considered further as their influence on overall stress-strain behavior is minor.

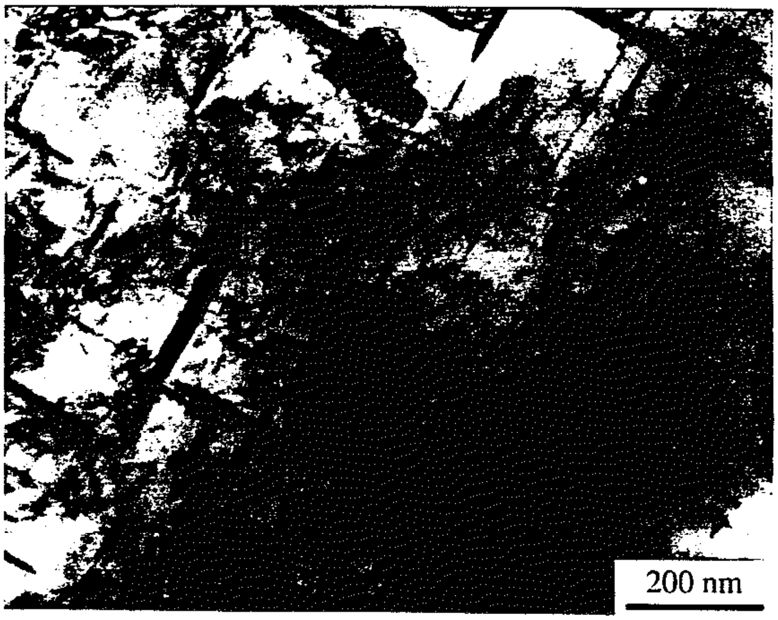

Figure 4a: Two-beam bright-field TEM micrograph obtained from an undeformed specimen

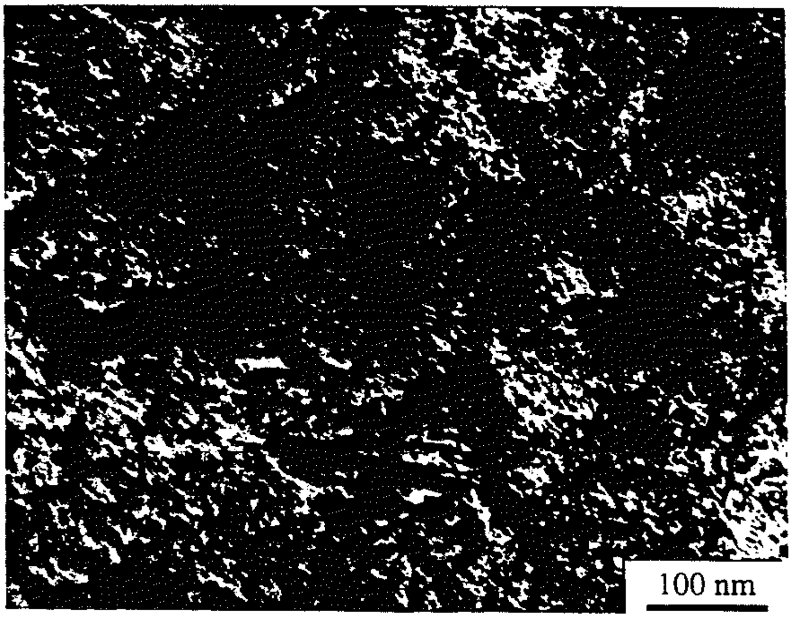

Figure 4b: g/3g weak-beam dark-field TEM micrograph showing that both coarse and fine θ precipitates are present in undeformed samples. Note that for ease of comparison the contrast of this image has been reversed

Figure 4a shows that plate-like coherent precipitates are present in the undeformed condition. However, weak-beam dark-field microscopy also revealed the presence of very fine θ precipitates as displayed in Figure 4b. The precipitates occupy the faces of the cubic lattice, {100} planes, as shown in Figure 5. Figure 4a demonstrates that the overall mobile dislocation density is very low thereby indicating that few artifacts were introduced during sample preparation. In addition, geometrically necessary dislocations were also observed at the θ' - matrix interface, but are out of contrast in Figures 4a and b.

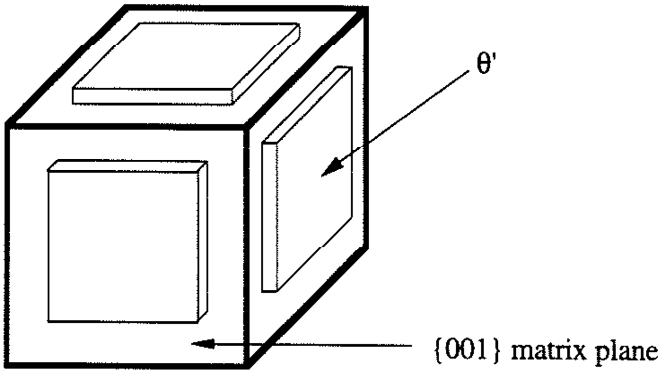

Figure 5: Schematic of Al_2Cu precipitates on the cubic lattice.

3.3 Effect of Solidification Rate on the Microstructure

As mentioned in section 3.1, the different solidification rates experienced in the wedge casting result in different SDAS and subsequently different microstructures through the wedge. For example, a solidification time of 60s. results in a SDAS of approximately 30μm, a time of 725s. in a SDAS of approximately 60μm, and a solidification time of 3100s. results in a SDAS of approximately 90μm. When focusing on a specific engine component, such as a cylinder head, the most highly stressed region of the cylinder head is usually the valve bridge area, as discussed in more detail later. As the wall thickness is usually the valve bridge area, as discussed in more detail later. As the wall thickness is relatively small in this area, cooling rates during solidification are high, resulting in a fine microstructure with small SDAS (≈30μm). Figures 6a to c show that changing the solidification conditions affects the SDAS. In addition, the morphology of the intermetallics and the level of porosity are both altered substantially with changing solidification rates.

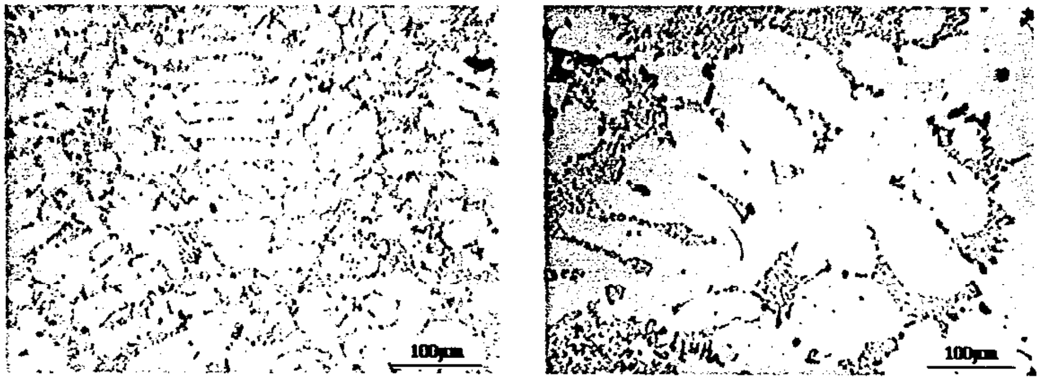

a) SDAS is ≈30μm

b) SDAS is ≈60μm

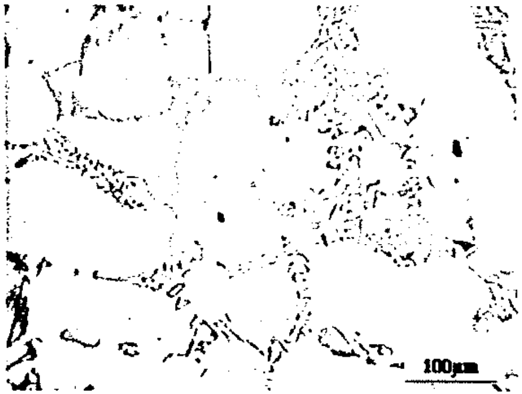

c) SDAS is ≈90μm

Figures 6a-c: Variation in microstructure as a result of different cooling rates during solidification.

drastically affect the cyclic softening behavior of the alloy. Material with large (≈90μm) SDAS not only fails after considerably fewer cycles than the small SDAS, but also exhibits significantly faster cyclic softening. Note that the increase in cyclic softening rate in the large SDAS material occurs despite the lower initial strength.

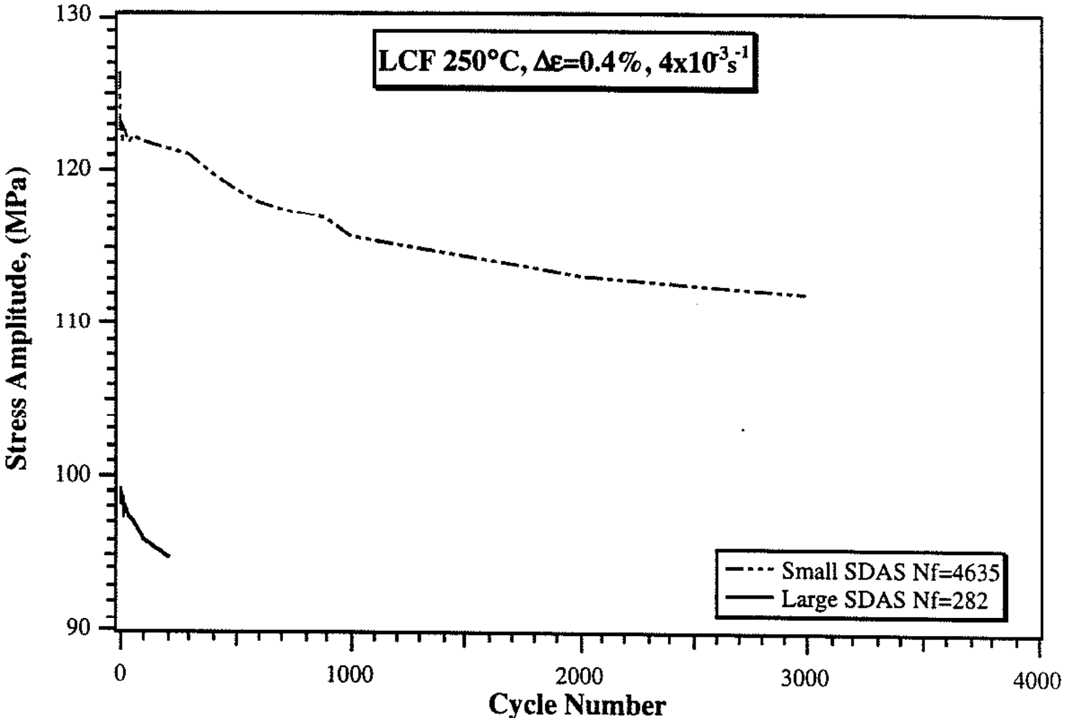

Figure 7: Effect of SDAS on cyclic stress-strain response at T=250°C and $\dot{\varepsilon}=4\times10^{-3}s^{-1}$. SDAS is ≈30μm ("small") and ≈90μm ("large"), respectively.

Figures 8a and b show TEM micrographs of fatigued samples with small and large SDAS, respectively. If compared to the undeformed material Figure 4b it becomes apparent that the θ precipitates have coarsened. Note that Figure 4b is at a higher magnification to clearly reveal the precipitates. Furthermore, the θ precipitates are already coarser in the large SDAS material (Figure 8b) than in the small SDAS material (Figure 8a). It should be noted that the actual appearance of the precipitates in the TEM foil largely depended on the actual foil thickness. However, the samples usually had rather large electron transparent areas, and thus many images were obtained to ensure the average coarsening observed for the two materials was indeed different.

Figures 8a and b were chosen such as to represent this average difference between the samples. Note, however, that both Figures 8a and 8b were obtained from samples cycled to failure. Thus, even if the difference in the coarsening of θ seen in Figures 8a and b, might not appear to be very large, this indicates substantially faster coarsening as the small SDAS has been cycled to approximately a ten times higher cumulative plastic strain than the large SDAS material.

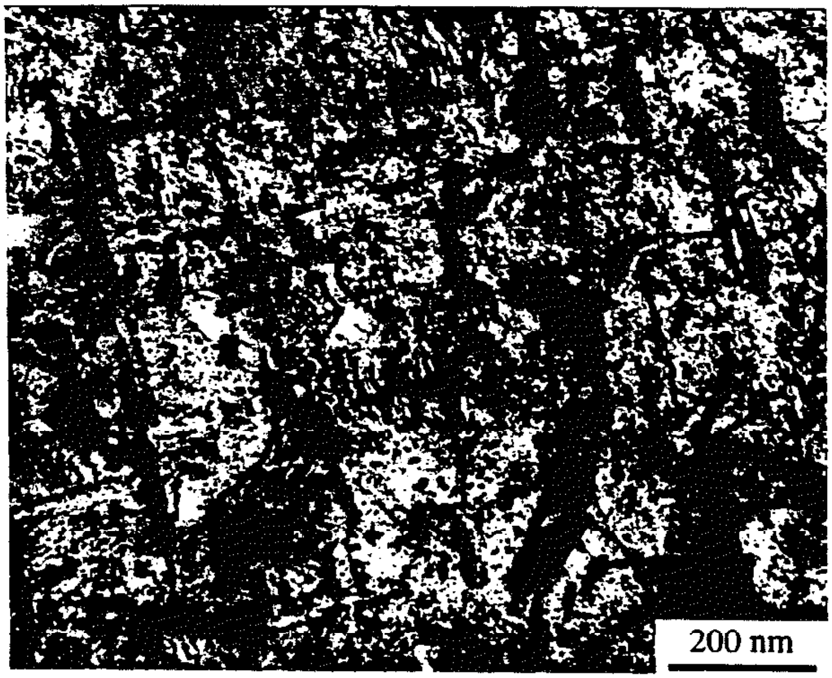

Figure 8a: g/3g weak-beam micrographs of fatigued samples with small SDAS

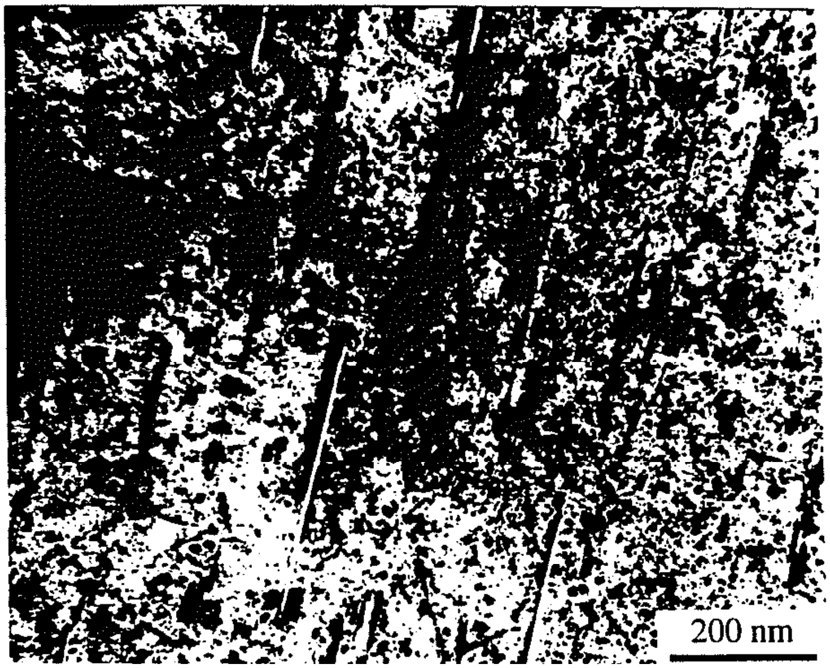

Figure 8b: g/3g weak-beam micrographs of fatigued samples with large SDAS

Deformation conditions as shown in Fig. 2. Note that for ease of comparison, the contrast of the images has been inverted.

4. STRESS-STRAIN MODEL AND DETERMINATION OF MODEL PARAMETERS

4.1 Overview of the Stress-Strain Model

The model presented for predicting the stress-strain behavior of this high temperature cast aluminum alloy is an experimentally based unified creep-plasticity constitutive model, previously developed by Slavik and Sehitoglu[1]. Two state variables, back stress and drag stress, are used to describe the material response and will be discussed later in more detail. A kinetic form of the flow rule is incorporated to calculate the inelastic strain rate components as a function of the state variables. A detailed description of the physical interpretation of the state variables in deviatoric stress space has been described in previous work[1].

The back stress, otherwise known as internal stress, describes the increase in a material's resistance to deformation with straining, e.g. due to dislocation pile-up resulting from dislocation interaction with barriers such as precipitates and other dislocations. The cyclic softening and hardening behavior of the material are governed by the change in drag stress. In terms of the microstructure, the drag stress change represents the effect of a developing microstructure on initial yielding behavior. The evolution of the two state variables follows a hardening and recovery formulation. The opposing functions work in conjunction with one another to determine the state variable evolution throughout a given deformation history.

4.2 Flow Rule

The flow rule used in this model is a kinetic form which relates the inelastic strain rate components to the state variables. The concepts of drag stress and yield strength are also connected through the flow rule. The functional form of the flow rule used in this model is given below

$$\dot{\varepsilon}_{ij}^{in} = \frac{3}{2} A f\left(\frac{\overline{\sigma}}{K}\right) \frac{S_{ij} - S_{ij}^{c}}{\overline{\sigma}} \tag{1}$$

where $\dot{\varepsilon}_{ij}^{in}$ is the inelastic strain rate, A is a material constant, K is the drag stress, $\overline{\sigma}$ is the effective stress, S_{ij} is the deviatoric stress, and S_{ij}^{c} is the deviatoric back stress. The effective stress is given as $\overline{\sigma} = \left[\frac{3}{2}\left(S_{ij} - S_{ij}^{c}\right)\left(S_{ij} - S_{ij}^{c}\right)\right]^{1/2}$, where the deviatoric quantities are given as $S_{ij} = \sigma_{ij} - \frac{1}{3}\delta_{ij}\sigma_{kk}$ and $S_{ij}^{c} = \alpha_{ij} - \frac{1}{3}\delta_{ij}\alpha_{kk}$. The flow function, $f\left(\frac{\overline{\sigma}}{K}\right)$, depends upon the active deformation mechanism such as power law creep, plasticity, or diffusional flow. This flow function is well motivated by Ashby's deformation mechanism maps[21]. The second term, $S_{ij} - S_{ij}^{c}$, determines the direction of the strain rate.

The flow rule is determined directly from isothermal experiments conducted at constant strain rates. Tensile tests with temperatures ranging from 20°C to 250°C and strain rates of either $5\text{x}10^{-5}s^{-1}$ or $5\text{x}10^{-2}s^{-1}$ were used to determined the flow rule in conjunction with isothermal fatigue tests at 250°C with a strain rate of $5\text{x}10^{-5}s^{-1}$ and 20°C at $5\text{x}10^{-3}s^{-1}$ and creep experiments at temperatures of 250°C and 300°C, see Figure 9. The first step in establishing the flow rule is to determine the yield strength and inelastic strain rate for each test as shown in Figure 9. The smaller the inelastic strain offset, the closer the offset yield strength to the actual yielding value of the material since the microstructure will not have changed significantly from its initial state. Since we are interested in small strain behavior, the proportional limit (0% strain offset) was used to obtain the yield strength as opposed to using a small inelastic strain offset yield strength. Since the data was available in digital format, it was possible to extract the proportional limit without ambiguity.

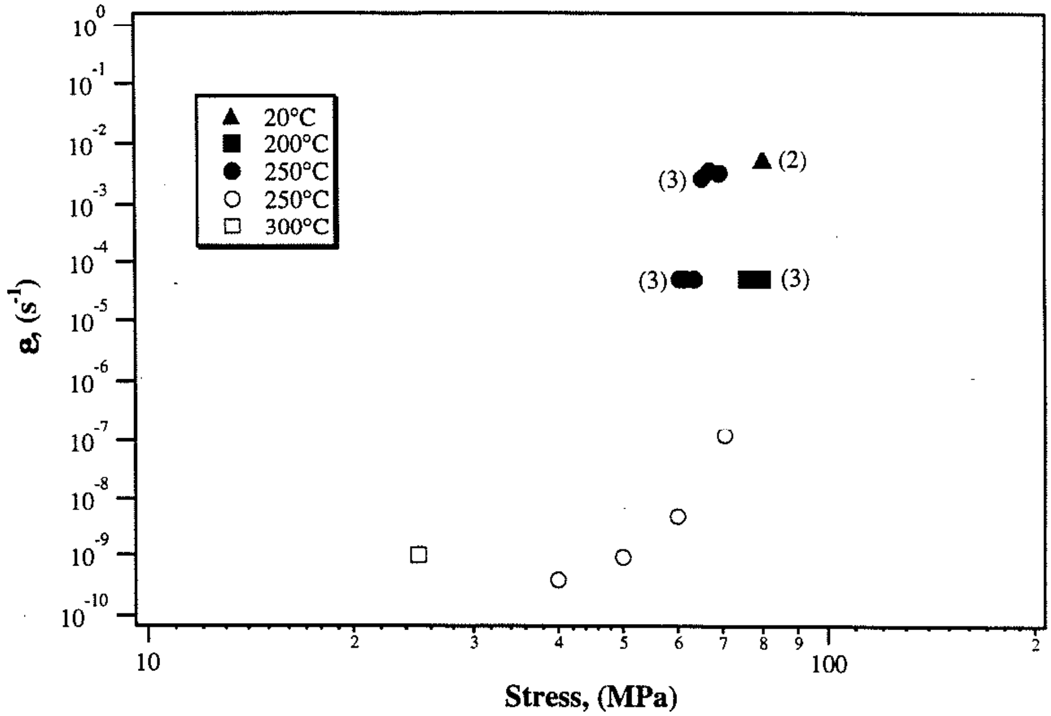

Figure 9: $\dot{\varepsilon}^{in}$ vs. σ plot for experiments used to determine the flow rule. Open symbols denote creep stress, full symbols represent proportional limit obtained from monotonic tensile tests or the initial loading part in case of fatigue tests.

* Numbers in brackets next to symbols indicate the number of tests in cases where individual data points overlap.

To determine the appropriate forms of the flow rule for the different deformation mechanisms, the yield strengths in Figure 9 must be normalized for different temperatures. The initial drag stress at the intersection point of the transition from power law creep to plasticity, K_0, was chosen as the normalizing parameter. For temperature regimes in which the available data did not exhibit a transition in deformation mechanisms, K_0 could be determined by taking $K_0/E=$ constant, where E is the elastic modulus. Since the elastic modulus is dependent upon temperature, K_0 can be also be established as a function of temperature and then used to normalize the experimental data which shows no observable intersection of deformation mechanisms in the different temperature regimes.

The results of the normalizing technique are shown in Figure 10 and display the distinctly different deformation mechanisms of power law creep and plasticity. As seen from Figure 10, the plasticity regime dominates for combinations of large stresses and high strain rates whereas power law creep dominates for lower stress and lower strain rates. The corresponding forms of the flow function for the two deformation mechanisms are

$$f\left(\frac{\overline{\sigma}}{K}\right)=\left(\frac{\overline{\sigma}}{K}\right)^{n_1} \qquad \text{when } \left(\frac{\overline{\sigma}}{K}\right) < 1.0 \tag{2a}$$

$$f\left(\frac{\overline{\sigma}}{K}\right)=\exp\left[\left(\frac{\overline{\sigma}}{K}\right)^{n_2}-1\right] \qquad \text{when } \left(\frac{\overline{\sigma}}{K}\right) \geq 1.0 \tag{2b}$$

where n_1 and n_2 are respectively the power law creep and plasticity exponents.

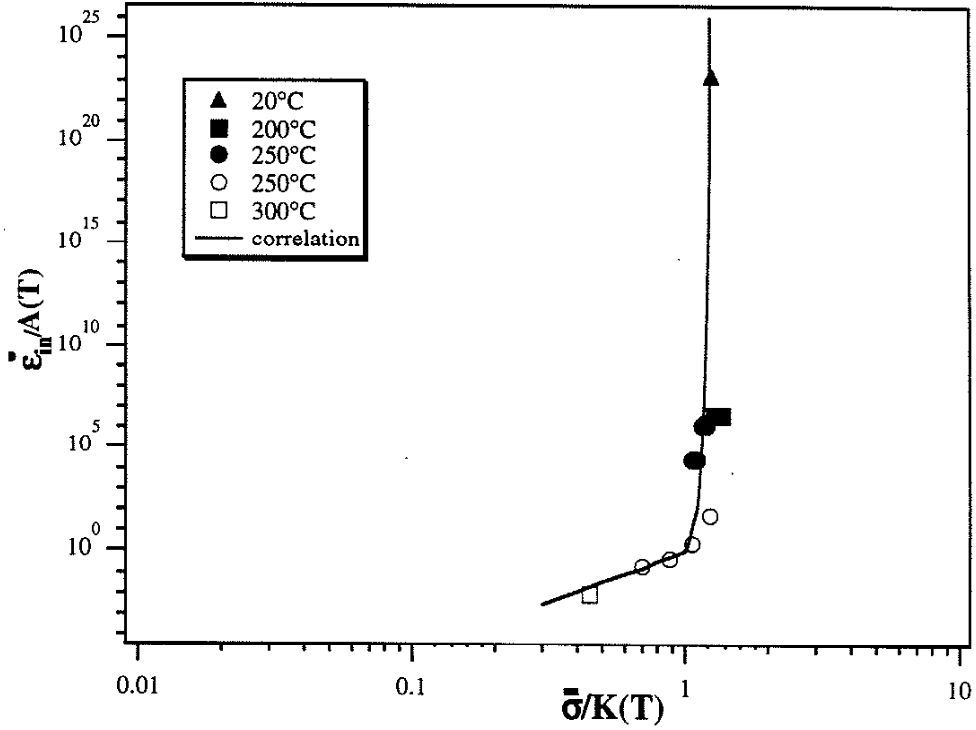

Figure 10: Correlation between flow rule and experiments.

4.3 Evolution of the Back Stress

The evolution of the back stress state variable is modeled as

$$\dot{S}^c_{ij} = \frac{2}{3} h_\alpha \dot{\varepsilon}^{in}_{ij} - \left[r^D_\alpha\left(\dot{\bar{\varepsilon}}^{in}_{ij}\right) + r^s_\alpha \right] S^c_{ij} \qquad (3)$$

where $\dot{S}^c_{ij}$ is the back stress rate, $\dot{\bar{\varepsilon}}^{in}_{ij}$ is the effective inelastic strain rate, h_α is the back stress hardening function, and r^D_α and r^s_α are respectively the dynamic and static back stress recovery functions. The effective inelastic strain rate is given as $\dot{\bar{\varepsilon}}^{in}_{ij} = \left(\frac{2}{3}\dot{\varepsilon}^{in}_{ij}\dot{\varepsilon}^{in}_{ij}\right)^{1/2}$. The hardening function, h_α , describes the evolution of the back stress during high strain rate experiments and acts to increase the back stress. In a converse manner, r_α tends to decrease the back stress to zero with increasing temperature or time.

The hardening function is then described by the following equation

$$h_\alpha = a_1 \exp\left[-\left(a_2\left(\alpha_0 + \bar{\alpha}\right)\right)^{a_3}\right] \qquad \text{when } \dot{\varepsilon}^{in}_{ij} \cdot S^c_{ij} > 0 \qquad (4a)$$

$$h_\alpha = a_1 \exp\left[-\left(a_2\left(\alpha_0 - \bar{\alpha}\right)\right)^{a_3}\right] \qquad \text{when } \dot{\varepsilon}^{in}_{ij} \cdot S^c_{ij} \leq 0 \qquad (4b)$$

in which a_1 is a material constant, a_2 and a_3 are material parameters which are functions of temperature, and α_0 is a constant back stress offset value since a cyclic experiment is utilized in comparison with a montonic tensile experiment. The effective back stress is defined as $\bar{\alpha} = \left(\frac{3}{2} S^c_{ij} S^c_{ij}\right)^{1/2}$. Due to changes in the microstructure over time, a_1, a_2, and a_3 subsequently evolve as functions of time, as seen in Appendix A. Before calculating the hardening parameters, an approximate determination of the back stress must be calculated from either monotonic tests or from the first reversal of a cyclic test.

A cyclic test at room temperature with a strain rate of $5\text{x}10^{-3}\text{s}^{-1}$ and a strain range of 0.6% was used for the determination of h_α. At room temperature the thermally activated recovery term becomes negligible and thus h_α can be determined from a room temperature cyclic or monotonic tensile test. From a stress-strain diagram, the back stress is defined as the yield stress subtracted from the current stress. The hardening function was then determined by plotting the back stress as a function of inelastic strain, thereby illustrating the evolution of the back stress. Figure 11 display the experimental points used to determine the hardening function.

A dynamic recovery formulation is incorporated in the description of the back stress evolution to effectively describe the recovery process which occurs simultaneously with deformation[22]. The static recovery term, r_α^s, is assumed to be equal to zero, leaving the dynamic recovery which can be expressed as:

$$r_\alpha^D = c(\overline{\alpha})^d\left(\dot{\overline{\varepsilon}}^{in}\right)^e \tag{5}$$

where c is a temperature dependent material parameter and, d and e are material constants (see Appendix A).

In the present study cyclic tests conducted at 250°C and tensile tests at 150°C and 250°C were used to determine the back stress recovery constants. As will be demonstrated later, substantial microstructural changes can occur during experiments, especially in the tests performed at low strain rate and high temperatures. Thus, the back stress recovery was masked largely by changes in the drag stress occurring under these conditions and the model gave a rather poor fit in the small scale yielding regime. As the problems of fatigue and engine application involve mostly small inelastic strains, it is mandatory to accurately simulate the stress-strain behavior at small strains.

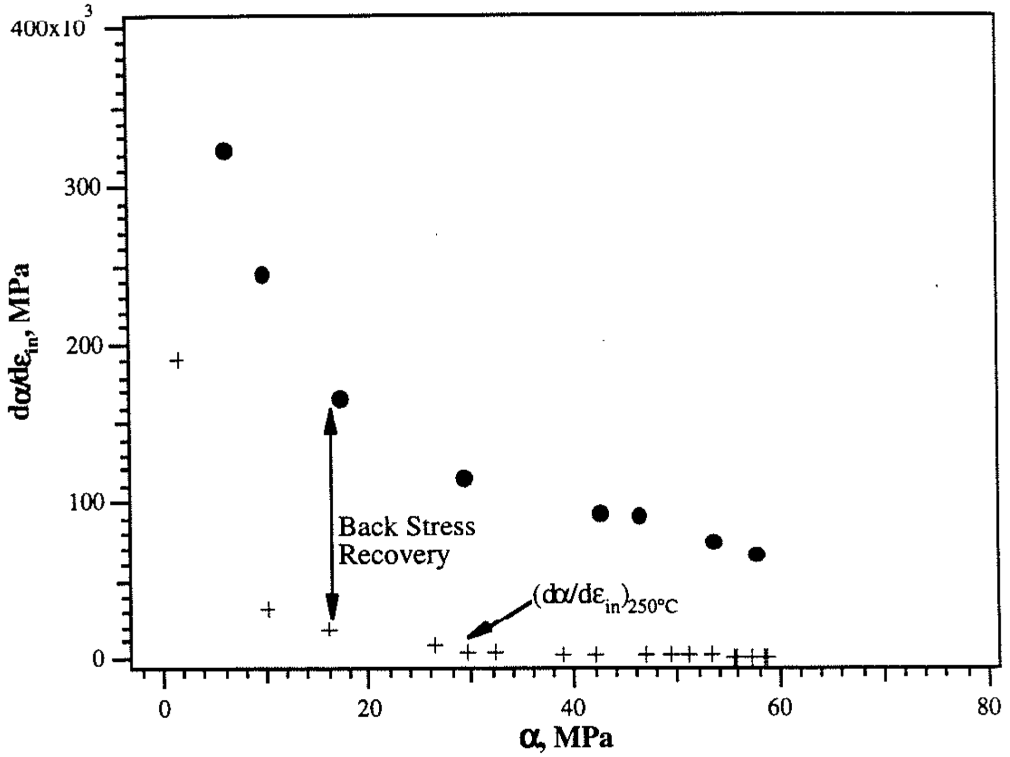

Figure 11: Graph demonstrating how the back stress recovery term $r_\alpha\left(\dot{\bar{\varepsilon}}_{ij}^{in}\right)^e$ is obtained as a function of back stress. The specific test shown was conducted at an inelastic strain rate of 5 x $10^{-5}s^{-1}$.

By rearranging Eq. 3, one can obtain the back stress recovery function from an analysis of the stress-strain response, as shown in Figure 11. The stress-strain response curve of a cyclic test at 250°C, a strain rate of $5x10^{-5}s^{-1}$, and a strain range of 0.4% was analyzed to determine the constants c, d, and e. A second test is then needed to determine the temperature dependence of c. The corresponding temperature dependent form of c is given in Appendix A.

4.4 Evolution of the Drag Stress

The evolution of the drag stress is modeled as

$$\dot{K} = h_k - r_k + \Theta T \tag{6}$$

where $\dot{K}$ is the drag stress rate. The drag stress hardening term h_k represents hardening or softening due to plastic deformation. The drag stress recovery term r_k governs the change in the drag stress caused by microstructural changes resulting from high-temperature exposure. The theta-term, $\dot{\Theta}$, represents the temperature dependence of the drag stress, as described later.

The drag stress hardening function h_k is given by

$$h_k = B(K_{sat} - K)\dot{\bar{\varepsilon}}^{in} \tag{7}$$

where B and K_{sat} are material constants which can be determined from isothermal experiments designed such that the drag stress recovery term is negligible. In the present study, fatigue tests conducted at a high strain rate ($\dot{\varepsilon}$=5x10^{-3}s^{-1}) were used to establish the material constants. Firstly, the yield stress range ($2\bar{\sigma}$) as a function of cycle number was obtained from the hysteresis loops. As the inelastic strain rate is known, the current value of K can be obtained by inverting Eq. (1).

The saturated value of K, K_{sat}, is obtained from a cyclically saturated hysteresis loop. Rearranging and integrating Eq. (7) indicates that the hardening (or softening) rate B can be obtained from the slope of a plot of $|K_{sat} - K|$ vs. the cumulative plastic strain as illustrated in Figure 12. Fatigue experiments conducted at both room-temperature and 250°C, yielded similar values for the material constant B. This result indicated that the hardening rate B is approximately independent of temperature.

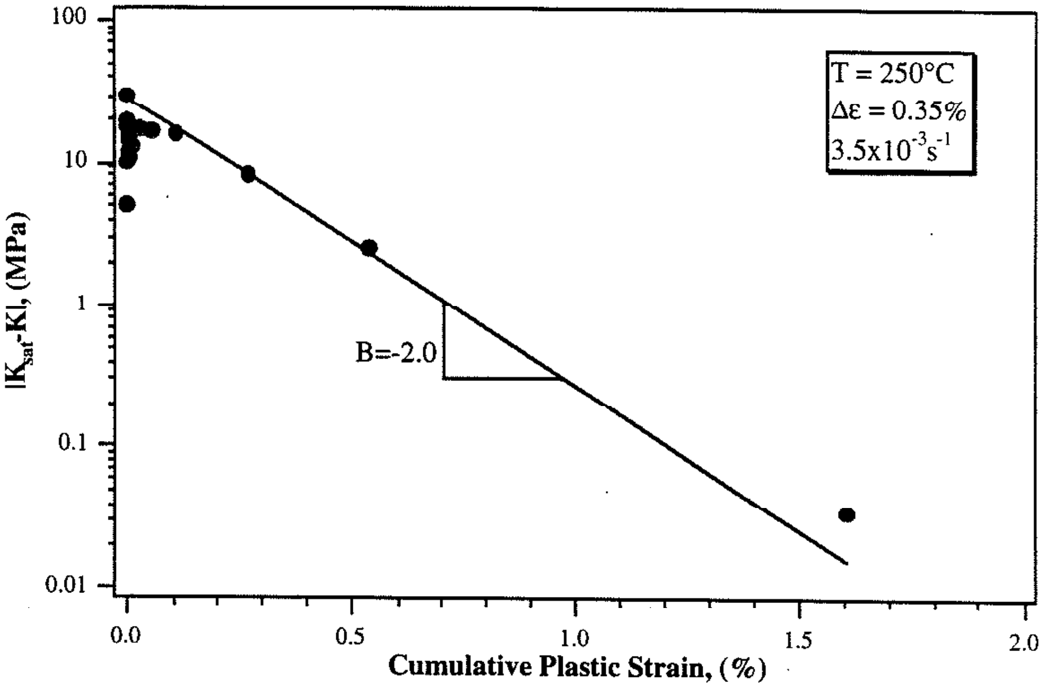

Figure 12: Graph to determine the drag stress hardening/softening rate B.

* Note that an average value of B obtained from both room temperature and high-temperature fatigue tests is used in this graph.

The effect of microstructural changes on the drag stress are represented by the recovery term r_k. Such effects are most pronounced at high temperatures and low strain rates. In earlier studies[18], r_k was determined from the stress-strain response of cyclically pre-deformed and subsequently heat treated material. In the present study, undeformed samples were used in place of the cyclically pre-deformed samples. In these experiments, the samples were exposed to temperatures of 100°C, 180°C and 250°C, respectively, for exposure times of up to 1000h. After thermal exposure and subsequent air cooling to room temperature, the yield stress was determined from room temperature tensile tests. The recovered value of K at room temperature (K^*) was then obtained from these tests by assuming that

$$\frac{K^*}{K_o} = \frac{\overline{\sigma}_{i+1}}{\overline{\sigma}_i} \tag{8}$$

where $\frac{\overline{\sigma}_{i+1}}{\overline{\sigma}_i}$ is the ratio of the yield stress after and before recovery. Finally, using the temperature dependence term (Θ) of the drag stress, which was established earlier, the actual value of K at the thermal exposure temperature is obtained. From these measurements the recovery function

$$r_k = B_3(K - K_{rec}) \tag{9}$$

was established. K_{rec} is the fully recovered value of the drag stress at a given temperature and B_3 governs the rate of drag stress recovery. Similar to the drag stress hardening rate, B_3 can be obtained from a plot of $(K - K_{rec})$ vs. thermal exposure time, see Figure 13.

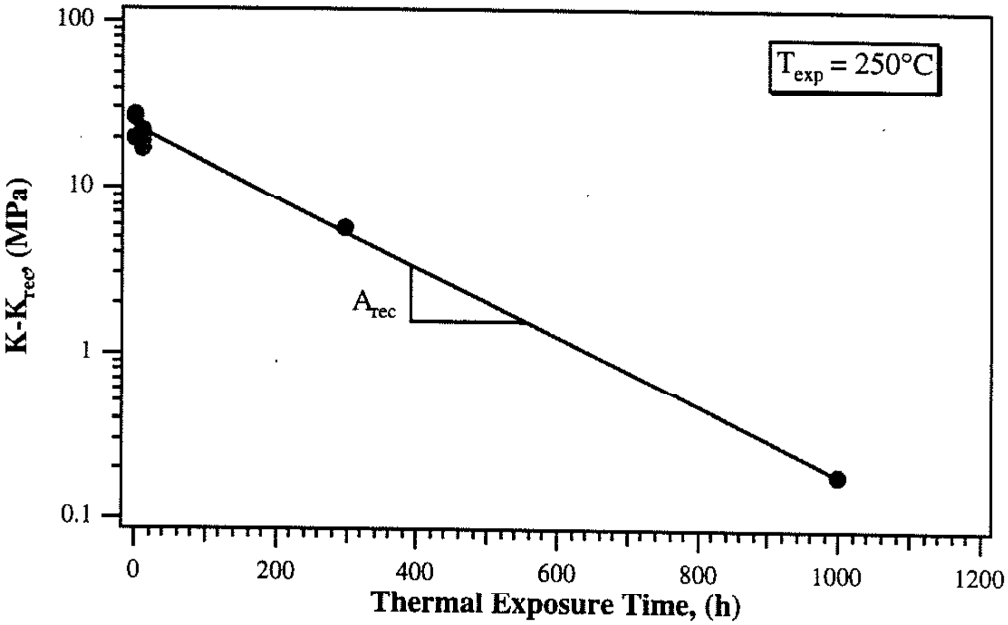

Figure 13: Determination of material parameters describing the drag stress recovery

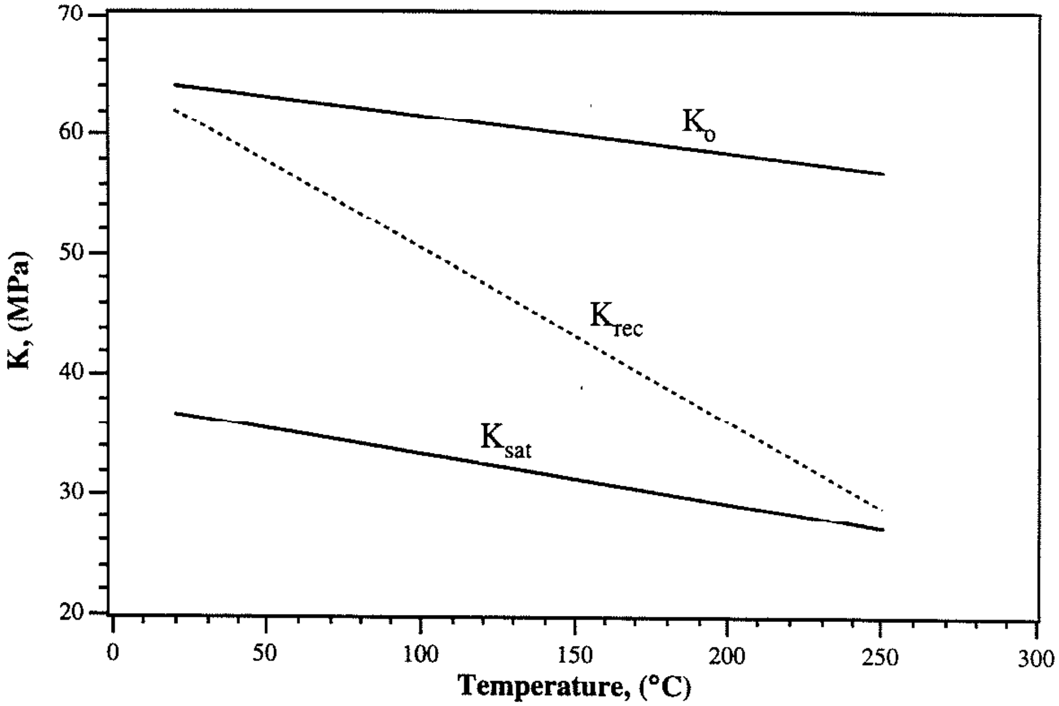

Figure 14: Temperature dependence of the initial drag stress (K_o), the saturated drag stress (K_{sat}) obtained in cyclic saturation and the recovered drag stress (K_{rec}) after thermal exposure.

Figure 14 summarizes the temperature dependence of the drag stress. Note that the drag stress decreases substantially as a result of either cyclic deformation (K_{sat}) or high-temperature exposure (K_{rec}). Such a large change in drag stress indicates pronounced microstructural changes. As seen in Figure 15, thermal exposure at high temperatures and long periods of time has caused extreme coarsening of the precipitates. The amount of microstructural change is best seen by comparing Figure 15 with the initial microstructure shown in Figures 4. From Figure 15 it is obvious that the coarse precipitates are no longer effective barriers to dislocation motion. Note that the formation of large areas that are almost free of precipitates are balanced by the formation of large precipitates. The latter tend to cluster, which is, however, only visible in low magnification micrographs.

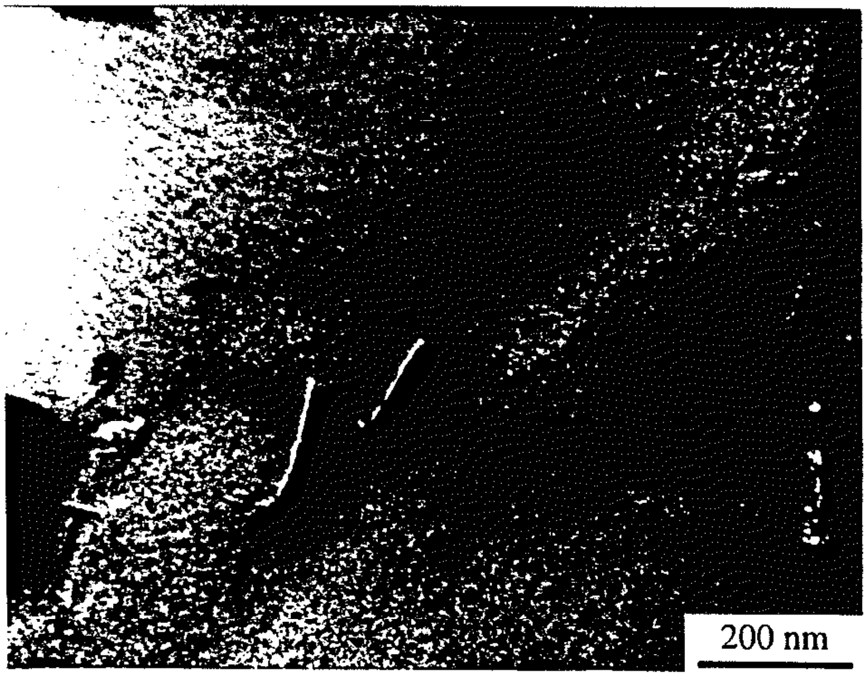

Figure 15: g/3g weak-beam dark field image showing dislocations moving almost unhindered by precipitates after the material has been exposed at 250°C for 1000h. Compare with Fig. 1. Note that both Fig. 8 and Fig. 1 are to the same scale.

Similarly, the cyclic softening observed in the fatigue experiments is caused by detrimental microstructural changes. These changes are most pronounced at high temperatures and slow strain rates. Figure 16 depicts the microstructure of a sample cycled at a low strain rate of $5\text{x}10^{-5}\text{s}^{-1}$ at a temperature of 250°C. Under these conditions the microstructure has coarsened substantially as compared to the undeformed microstructures of Figures 4. Selected area diffraction patterns indicated that the θ' precipitates have not only coarsened but also started to deviate from the initial {100} habits. Since thermal exposure and high temperature, low strain rate fatigue finally result in very similar microstructures, i.e. coarse precipitates, the values of K_{sat} and K_{rec} should also be similar. Figure 14 indeed indicates that within the experimental scatter both K_{sat} and K_{rec} are identical at 250°C.

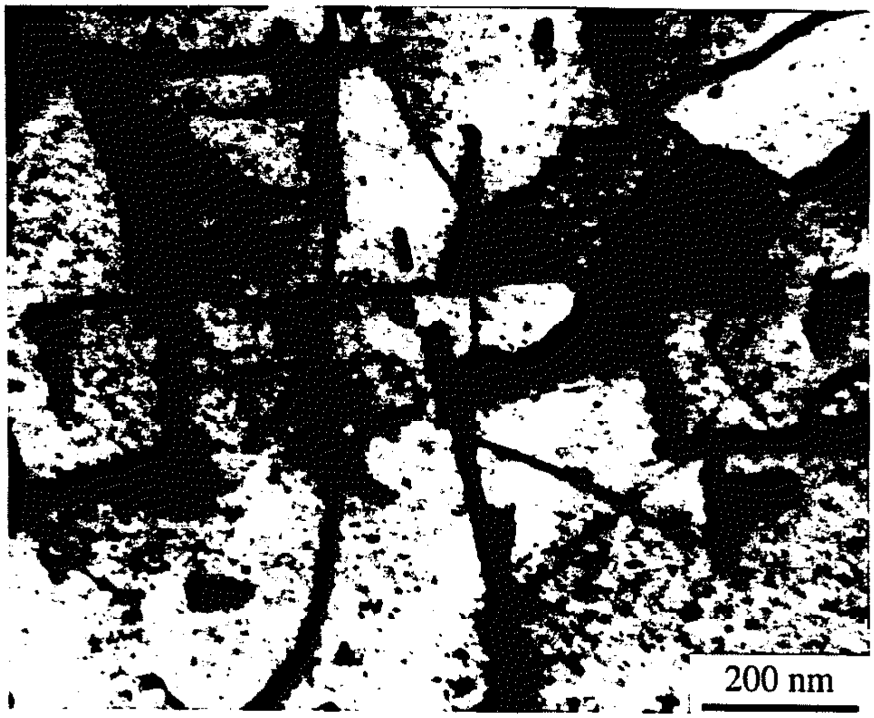

Figure 16: TEM micrograph showing the microstructure of a sample fatigued for 4,782 cycles at 250°C, $\Delta\varepsilon$=0.25% and $\dot{\varepsilon}=5\mathrm{x}10^{-5}\mathrm{s}^{-1}$. Two-beam bright-field image.

At this point, it should be noted that the procedure described thus far assumes that the drag stress hardening and drag stress recovery are independent processes. However, the TEM studies indicated that both cyclic deformation and high-temperature exposure cause softening as a result of the same basic process, i.e. coarsening of the precipitates. In fact, it was observed that the pronounced cyclic softening seen in the low strain-rate high-temperature test could not be predicted based on the data obtained from the thermal exposure tests only. To match the experiments the model was modified to allow for higher drag stress recovery if deformation occurred in the plasticity regime, see Appendix A.

5. EXPERIMENTAL RESULTS AND SIMULATIONS

The first verification to determine if the presented constitutive model accurately models the mechanical behavior of Al 319 was to compare the correlations of experiments used to determine the material constants with the experimental data. The second verification method focuses on the abilities of the model to predict the mechanical response of the material when subjected to complex loading and temperature histories, such as thermo-mechanical fatigue, creep and isothermal fatigue with strain hold dwell periods. Chapter 6 details the predictive capabilities of the model and corresponding experimental results. The first set of simulations, illustrated in this chapter, provide an indication of how accurately the material constants and parameters function in the expected manner and work in conjunction with one another to simulate the material behavior.

5.1 Monotonic Tensile Experiments

The hardening and recovery effects can be most obviously seen by simulating the tensile experiments, as shown in Figure 17. The simulations were performed for experiments performed at 20°C, 150°C, and 250°C. The 150°C and 250°C tests were controlled at a strain rate of $5x10^{-5}s^{-1}$ and the 20°C test was conducted at $5x10^{-2}s^{-1}$. In all three cases, the simulations were continued to a strain of 2% since the experimental tests had failed in the vicinity of this strain value.

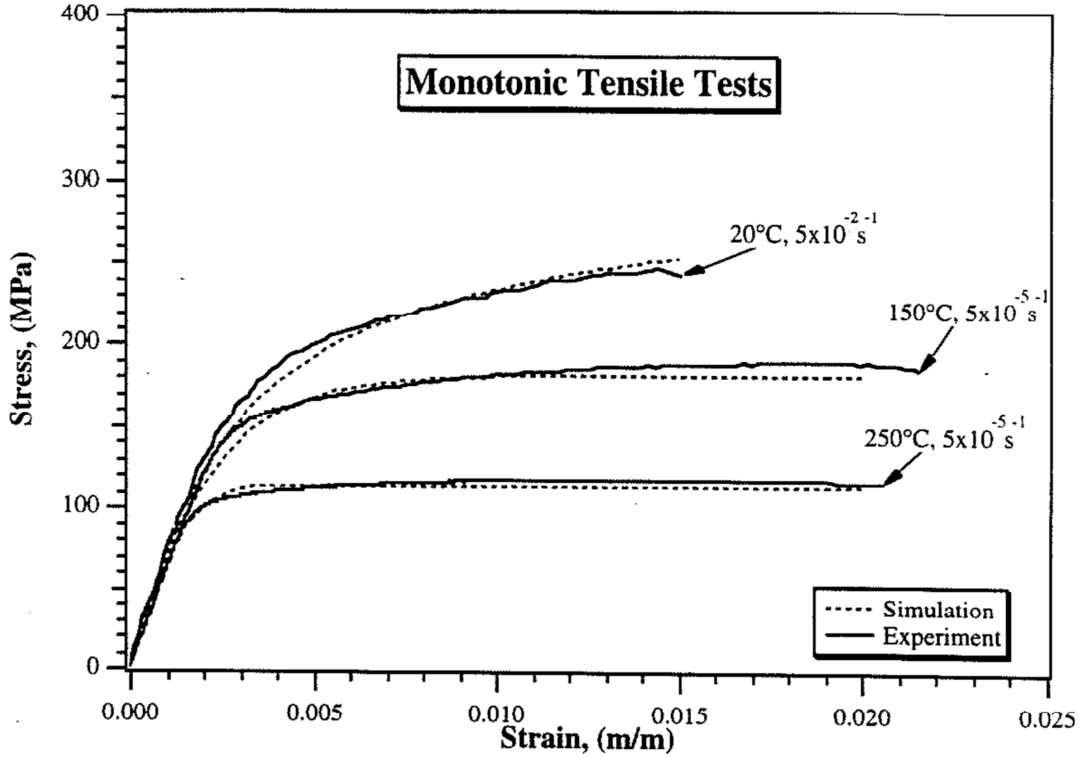

Figure 17: Comparison of experimental results and simulations for tensile tests at 20°C and $\dot{\varepsilon}=5\mathrm{x}10^{-2}s^{-1}$ and at 150°C and 250°C at $\dot{\varepsilon}=5\mathrm{x}10^{-5}s^{-1}$.

The model simulations corresponded closely to the experimental results. The most accurate correlation was seen for the room temperature tensile tests. This result would be expected since the room temperature tensile tests were used to determine the back stress hardening parameters. In this case, the hardening is the dominant mechanism in the evolution of the back stress, since the recovery term is thermally activated. On the other hand, the tests at 150°C and 250°C demonstrate the distinct affect of hardening and recovery working in conjunction to bring the material behavior to a saturated response. The hardening term works to increase the back stress, while the recovery term works to decrease the back stress rate to zero, i.e. to a saturated response.

As mentioned earlier, cast aluminum alloys experience different strain sensitivity regimes under different stress and strain combinations. The material is rate insensitive for combinations of high stress and fast strain rates, and rate sensitive for lower stresses and slow strain rates. Consequently, it is vital that the constitutive model possess the capability of modeling strain rate sensitive or insensitive behavior. To demonstrate this ability, monotonic tensile tests at 250°C were conducted at two different strain rates of $5\times10^{-5}s^{-1}$ and $10^{-6}s^{-1}$ and compared with the corresponding experimental results. It should be noted that the experiment at a strain rate of $10^{-6}s^{-1}$ was stopped at a strain of 2% and was not allowed to continue until failure.

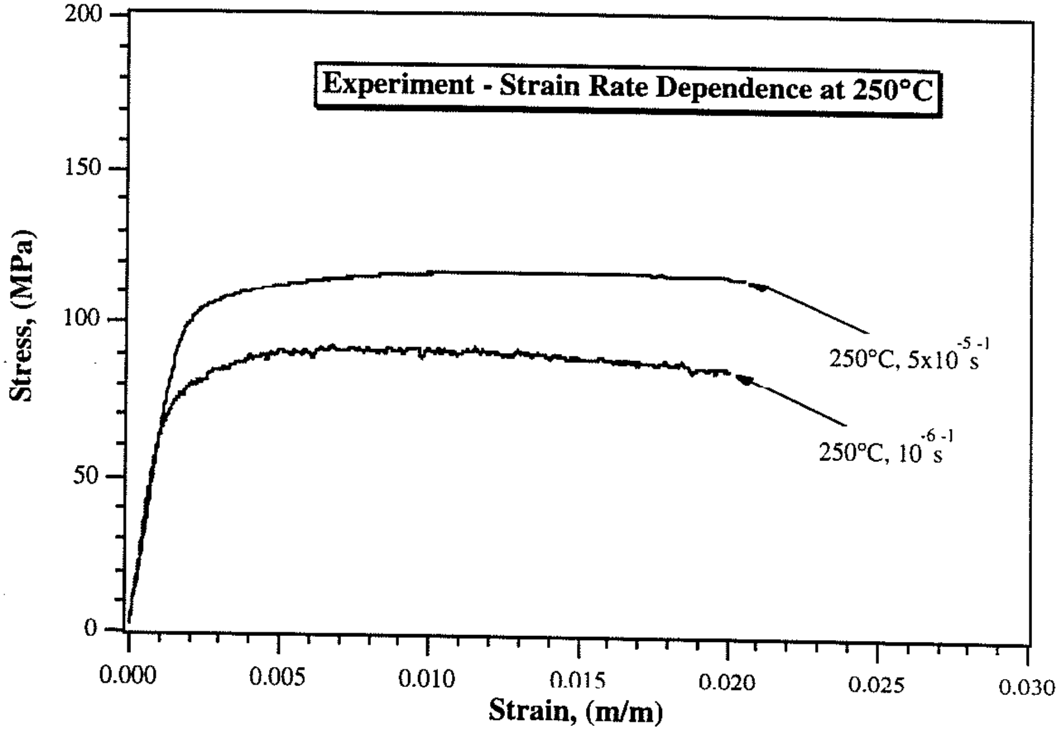

Figure 18a: Effect of strain rate on the stress response of the material. Comparison of experimental results at 250°C and $\dot{\varepsilon}=5\times10^{-5}s^{-1}$ and $\dot{\varepsilon}=10^{-6}s$

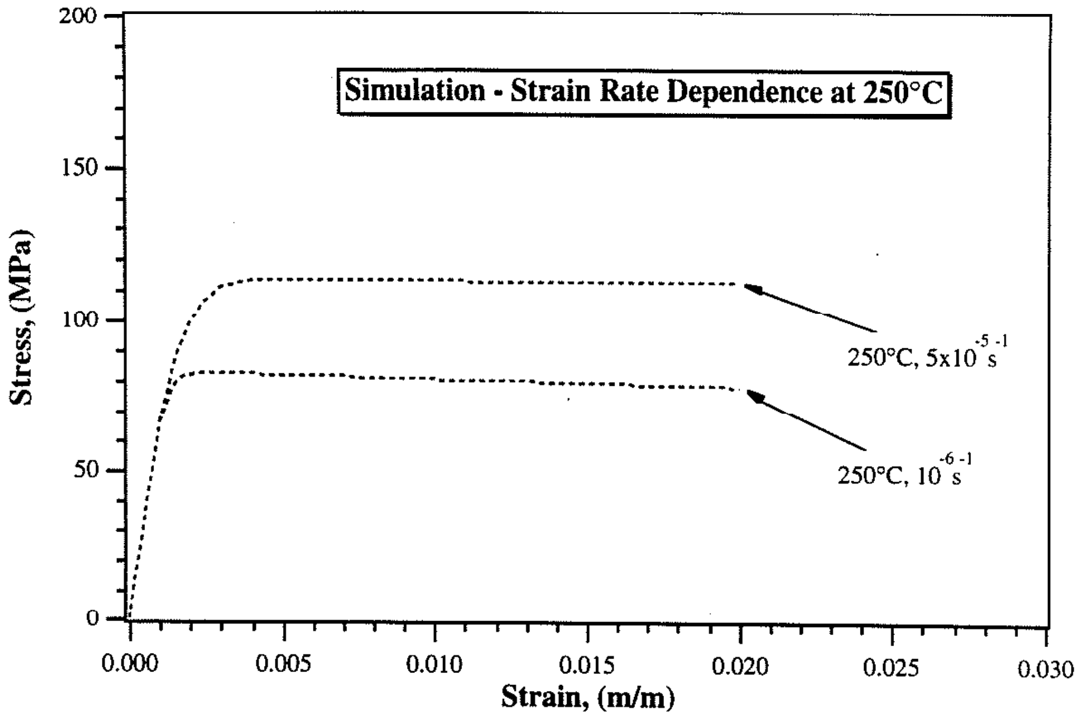

Figure 18b: Effect of strain rate on the stress response of the material. Comparison of simulations under identical conditions as experiments.

The results of the strain rate effect on stress-strain response are shown in Figure 18a for the experimental results and in Figure 18b for the simulations. At 250°C, the material demonstrates rate sensitive behavior as exemplified by the decrease in the yield stress as the strain rate decreases. One observation to note in the experiment and simulation at $10^{-6}s^{-1}$ is the decrease in strength after attaining the UTS, which is not as readily observed in the experiment at $5x10^{-5}s^{-1}$ which acquires a state of saturation. The combination of temperature and slower strain rate ($10^{-6}s^{-1}$) result in a material response which indicates pronounced microstructural changes, as previously mentioned, thereby resulting in the softening of the material.

5.2 Isothermal Fatigue Experiments

The transient cyclic stress-strain behavior must also be accurately captured by the model. Dependent upon a material's previous aging and deformation history, a material will cyclically soften or harden until it reaches a stable condition. The ability of the Al 319 alloy to attain a cyclically stable state is dependent upon the temperature, the strain rate, and the strain. Figure 19 displays one example of the model's ability to capture the transient cyclic behavior by comparing simulation and experimental results of an isothermal fatigue test at 250°C conducted at a strain rate of $5\times10^{-5}s^{-1}$ over a strain range of 0.4%.

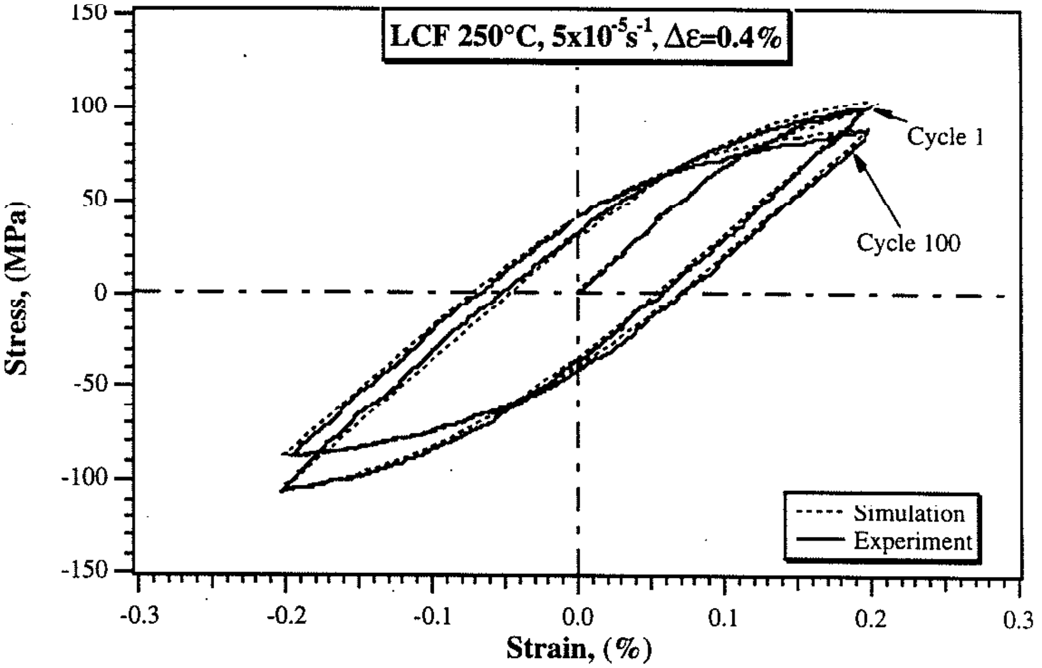

Figure 19: Effect of cyclic softening on stress response. Comparison of simulation and experimental results for low cycle fatigue experiment at 250°C, $\Delta\varepsilon$=0.4%, and $\dot{\varepsilon}=5\times10^{-5}s^{-1}$.

The results of the comparison and experiment are presented in Figure 19 for the initial loading, subsequent cycle and cycle 100. The model accurately represents the decrease in strength, the maximum and minimum stresses and the increase in plasticity exhibited during the experiment. Figure 19 depicts a decrease in the maximum and minimum stresses from cycle 1 to cycle 100 of approximately 15%. As previously mentioned, the transient behavior of the alloy depends upon a number of conditions. For this given experiment, the alloy never attained a steady-state but continuously softened until the failure criteria were satisfied.

5.3 Thermal Exposure Experiments

The objective of the final comparison, of the model simulations with experimental data used to determine the material parameters, is to determine the ability of the model to represent the effect of extended thermal exposure upon the material's subsequent response. The experimental test involved thermal exposure at 250°C for 1000 hour, air cool to room temperature, and then followed by a tensile test at room temperature. The strain rate for the tensile test was $5\times10^{-2}s^{-1}$. Figure 20 shows the results of the simulation and experiment. For comparison purposes, the experimental result at room temperature, performed on virgin material, is also displayed to demonstrate the significant effect of extended thermal exposure on material properties.

Figure 20 demonstrates that the model can predict the changing material response of the material under extended thermal exposure. When comparing the pre-exposure and post exposure tests, the ultimate tensile strength (UTS) experienced a decrease of approximately 100MPa due to extended thermal exposure at high temperature. The microstructural explanation for such a drastic degradation in material properties will be discussed in detail in Chapter 7.

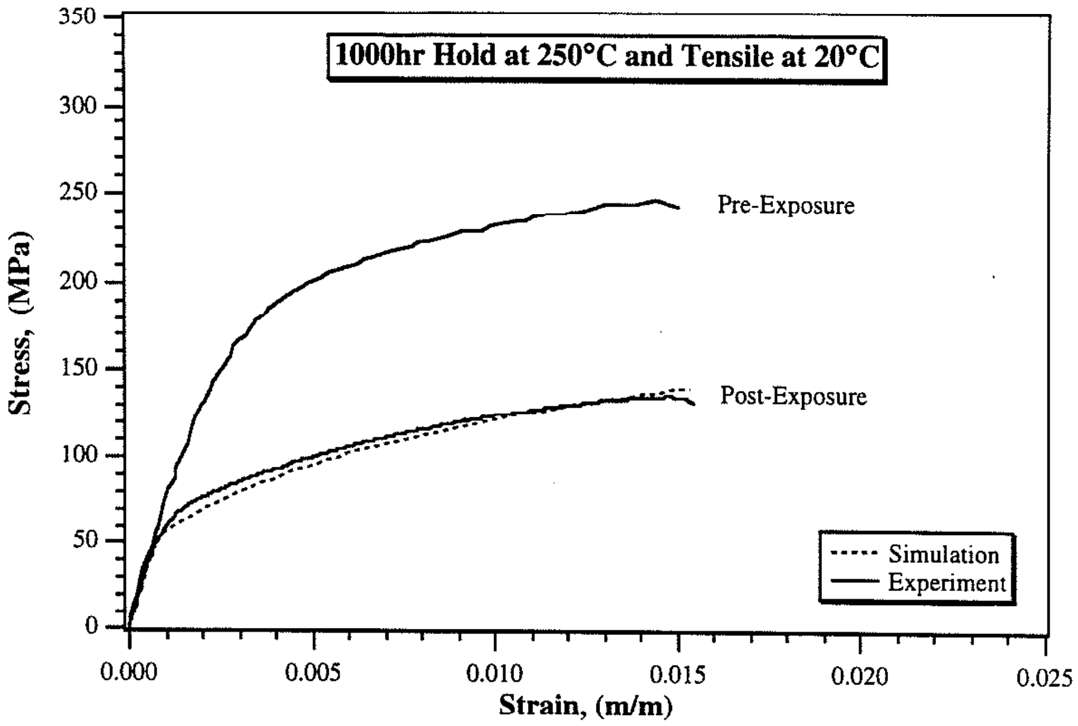

Figure 20: Effect of thermal exposure on stress response. Comparison of simulation and experimental results after thermal exposure at 250°C for 1000h and tensile test conducted at 20°C and $5x10^{-2}s^{-1}$.

As a first check on the model, Figures 17-20 demonstrate an accurate correspondence between the simulations and experiments. The following chapter analyzes the predictive capabilities of the model by comparing simulations with experiments which were completely independent of determining the material constants and the flow rule. The preceding simulations have demonstrated that the flow functions and material parameters are valid for simulating the material's response for the cases studied.

6. PREDICTIVE CAPABILITIES OF THE MODEL

6.1 Thermo-Mechanical Fatigue Experiments

During start-up of an engine the temperature in the valve bridge area of a cylinder head increases rapidly, while the surrounding water-cooled material constrains thermal expansion of the material. Consequently, thermal stresses increase and significant plastic deformation may occur, if the stresses exceed the compressive yield point at high temperatures. Similarly, upon cooling to ambient temperature, tensile stresses develop and a mechanical stress-strain hysteresis loop is obtained. During service, repeated start-up and shut-down cycles accumulate plastic strain and damage until finally resulting in thermo-mechanical fatigue (TMF). In the simple scenario outlined, the constraint caused by the water-cooled surrounding material causes the hot material to experience compressive stresses while the temperature in the valve bridge area is high. Consequently, emphasis was placed on out-of-phase tests (OP) in which the maximum temperature coincides with the maximum compressive mechanical strain and all tests were conducted at a constant strain rate of $5x10^{-5}s^{-1}$.

Since TMF tests are time consuming and expensive, the experiments are usually performed under conditions more severe than those experienced during service of an actual engine. Modeling of the stress-strain response under TMF conditions should thus help to define accelerated tests that can be used to predict fatigue life under service conditions.

Many thermal fatigue tests are performed under almost fully constrained conditions, i.e. the total strain on the sample during the thermal cycle is maintained close to zero by gripping the sample in a rigid frame. In the present study, independent temperature and closed-loop strain control were used to observe the material's response and the model's prediction over a wider strain range.

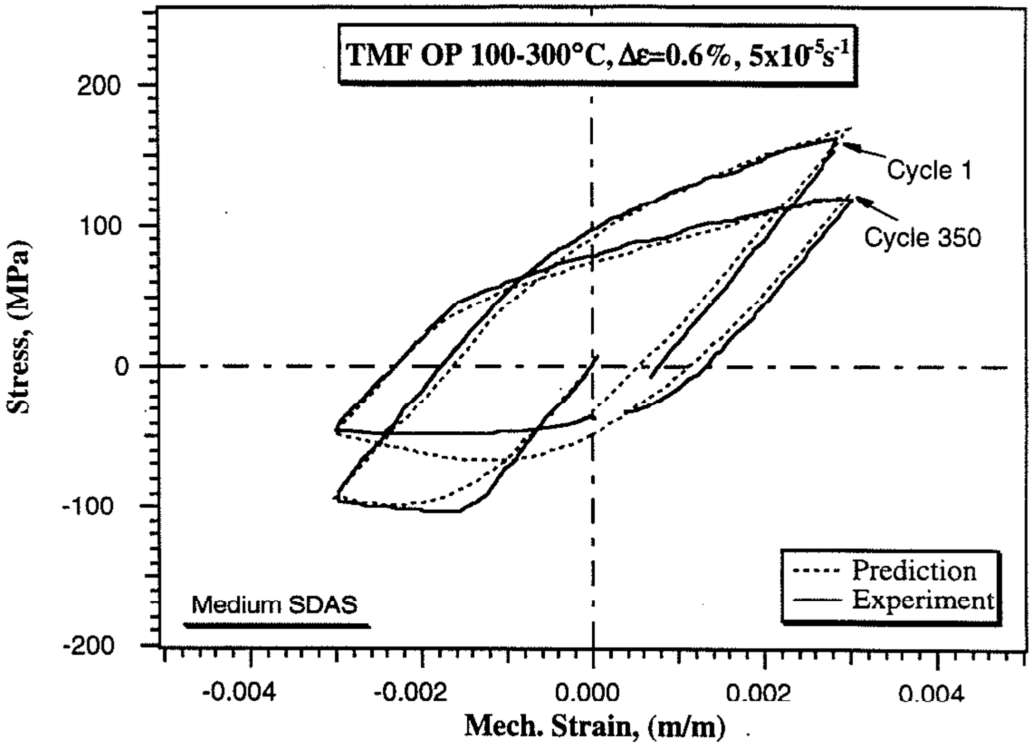

Figure 21: Predicted and experimental hysteresis loops from a TMF OP test conducted between 100 and 300°C and $\Delta\varepsilon=0.6\%$, and $\dot{\varepsilon}=5\text{x}10^{-5}\text{s}^{-1}$.

The experimental results of an OP TMF test are presented in Figure 21. The experiment was conducted at a strain rate of $5\text{x}10^{-5}\text{s}^{-1}$ with a temperature range of 100-300°C and a strain range of 0.6%. Figure 21 also includes the model prediction for these testing conditions and demonstrates that the model predicts the experimental hysteresis loops quite accurately. The results demonstrate that substantial plasticity develops in these experiments as a result of the rapid drop in yield strength due to the extremely high temperatures. Not only does the model accurately predict the hysteresis loops but also accurately predicts the significant drop in yield strength and increase in plasticity.

6.2 Strain Dwell Isothermal Fatigue Experiments

At high temperatures, substantial stress relaxation can occur during hold periods. To evaluate the models predictive capabilities, isothermal strain dwell experiments were performed with hold periods in either compression or tension. Figures 22a and 22b exhibit a comparison between model prediction and the stress-strain response recorded during an isothermal fatigue experiment with a two minute hold period in compression. The test was conducted at a high temperature of 250°C and a low strain rate of $5\times10^{-5}s^{-1}$, since microstructural changes are most pronounced under these conditions. Thus, the changes in hysteresis loop shape are expected to be greatest. As seen in Figures 22a and b the model quite accurately predicts all of the main features observed in the experiment. Note that the model not only the predicts the amount of stress relaxation but also predicts the significant increase in the plastic strain range observed after 20 cycles.

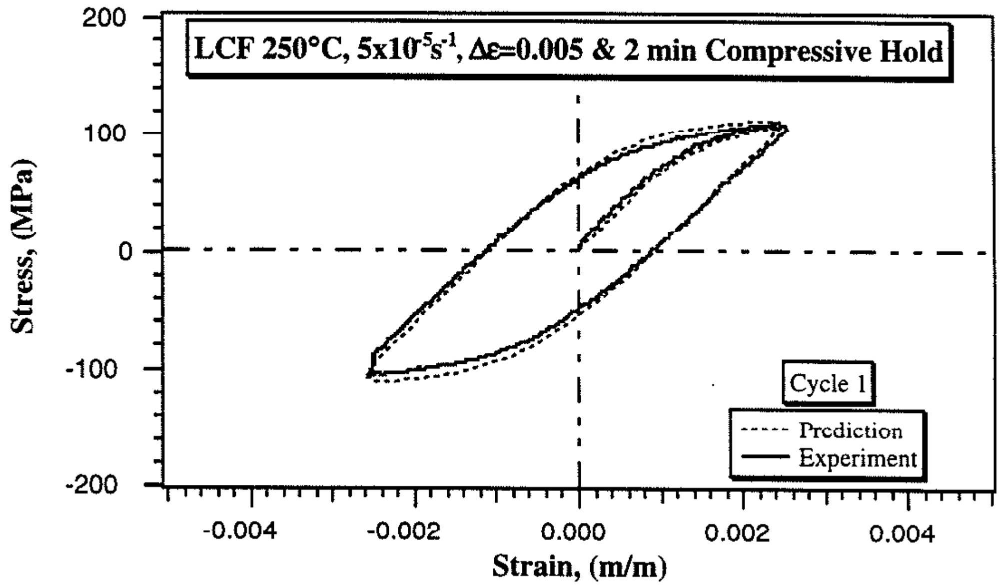

Figure 22a: Comparison of predicted stress-strain behavior in dwell test with experiment conducted at 250°C and $\dot{\varepsilon}=5\times10^{-5}s^{-1}$ with a 2 minute dwell period in compression. **N=1**

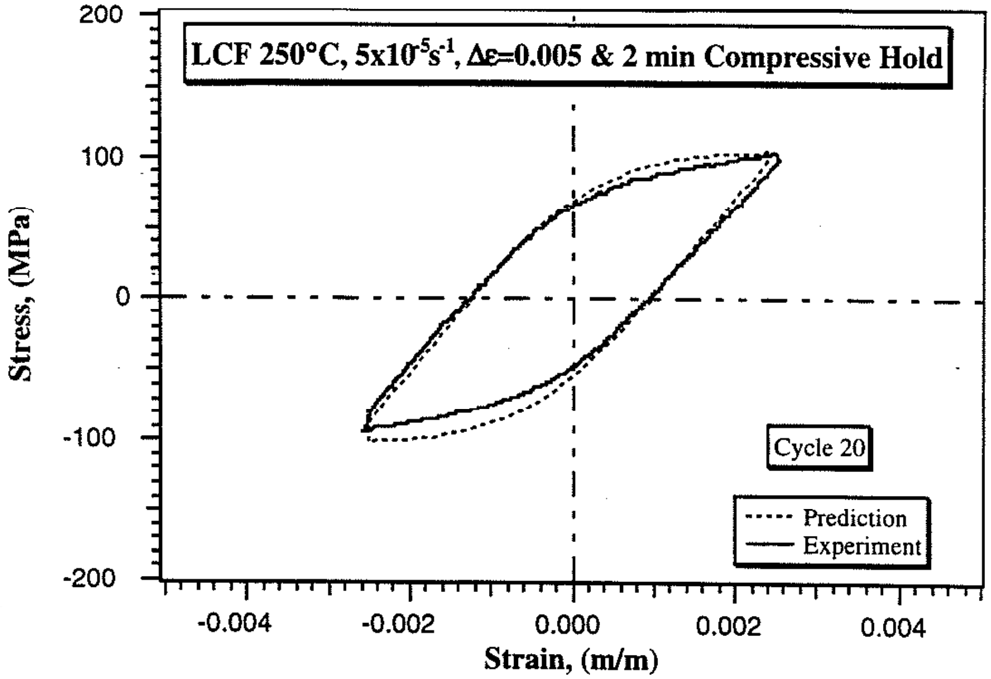

Figure 22b: Comparison of predicted stress-strain behavior in dwell test with experiment conducted at 250°C and $\dot{\varepsilon}=5\mathrm{x}10^{-5}\mathrm{s}^{-1}$ with a 2 minute dwell period in compression. **N=20**

The stress relaxation during the hold period is governed by the amount of back stress recovery, whereas the cyclic softening is controlled mostly by drag stress recovery. During a dwell test, the inelastic strain rate varies significantly along the hysteresis loop. Consequently, to obtain an accurate correlation between prediction and experiment, such as demonstrated in Figs. 22a and b, the model constants were established from tensile and fatigue tests which encompassed a wide range of inelastic strain rates.

6.3 Low Stress-High Temperature Creep Experiments

Except for the TMF tests, all experiments described thus far were conducted at temperatures of 250°C or lower. However, during TMF testing, temperatures in excess of 250°C comprise only a small portion of the cycle. Thus, all of the presented experiments can be considered as being conducted below the maximum temperature of 260°C used during the aging treatment. If the test temperature is increased beyond the aging temperature, the material strength decreases substantially and creep contributions dominate.

Figure 23 shows an example of a creep test conducted at 300°C and at a relatively high stress of 40 MPa. As expected, the creep curve displays initial transient creep behavior, followed by steady state creep and subsequently the creep rate increased with the transformation to tertiary creep. In contrast, creep experiments under low stresses exhibited a completely different behavior. Figure 24 displays the result of a creep experiment conducted at a low creep stress of 25 MPa. Following a small instantaneous positive strain during initial loading, the inelastic strain decreases under tensile load, i.e. the sample contracts. Then a positive strain builds before the inelastic strain again decreases at approximately 40 h. Such creep behavior was observed at creep stresses as high as 30MPa. From the flow rule (see Figure 10) the steady state creep rate at 300°C and 25 MPa is calculated to be approximately $3 \times 10^{-9} s^{-1}$. The unexpected creep behavior at low stresses indicates a substantial volume decrease as a result of microstructural changes. Therefore, creep tests at zero stress were performed to separate deformation-induced and temperature-induced effects on the creep response.

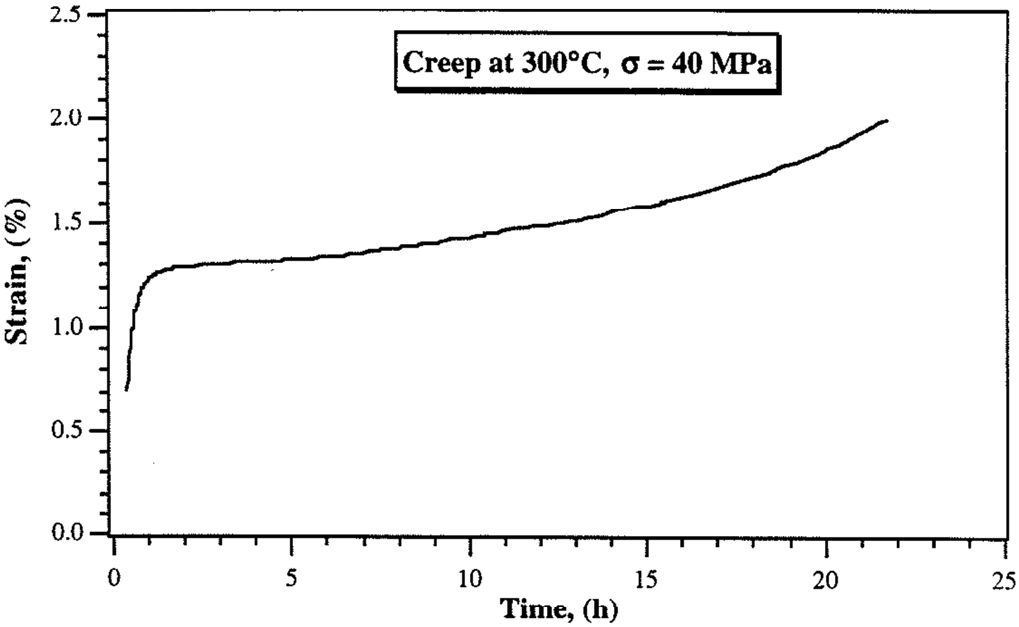

Figure 23: Creep strain as a function of time in a test conducted at a high creep stress and T=300°C for material with a SDAS of ≈60μm.

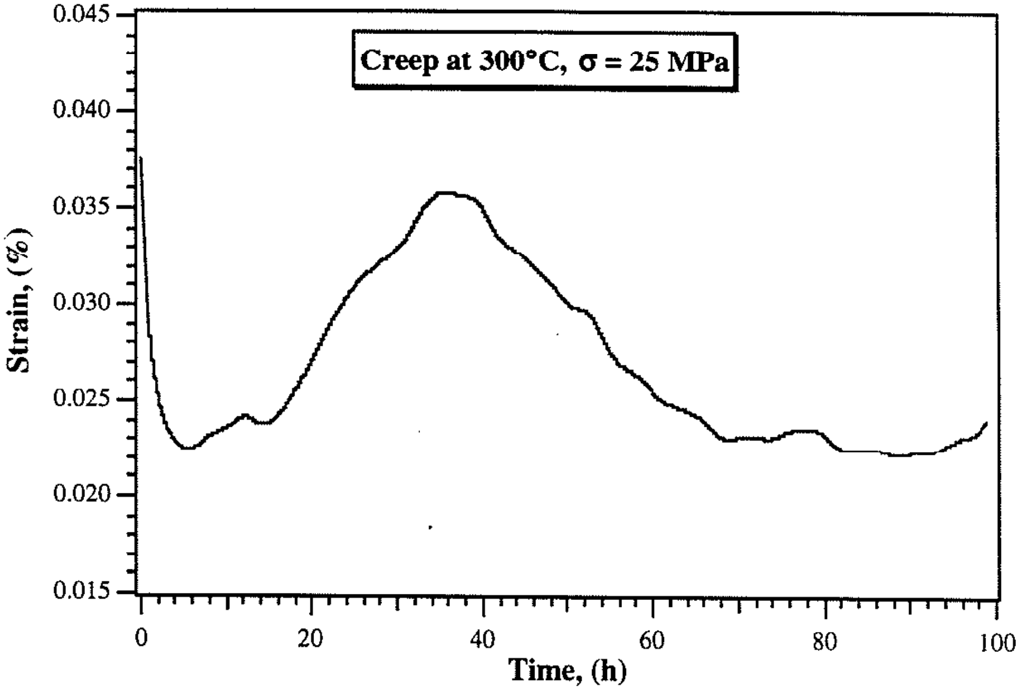

Figure 24: Creep curve obtained at a low creep stress and T=300°C. SDAS is ≈60μm.

Figure 25 illustrates that at a temperature of 300°C the inelastic strain in a zero-stress experiment first decreases rapidly and saturates at a value as large as -0.12%. Thus, the creep curve shown in Figure 24 is mostly dominated by the rapid decomposition of the θ' phase and to a much lesser extent by the applied tensile stress. However, due to the large contraction observed in Figure 25 it is likely that a second mechanism is present such as that caused by preferred orientation of the precipitates during solidification. As previously mentioned, the samples were machined from a wedge-shaped geometry with a controlled solidification front. Consequently, the precipitates may subsequently form in a preferred orientation due to the directionality of the dendrites during solidification. At this time, the underlying mechanisms for the observed behavior in Figure 25 are not fully understood and additional studies of this behavior are currently in progress.

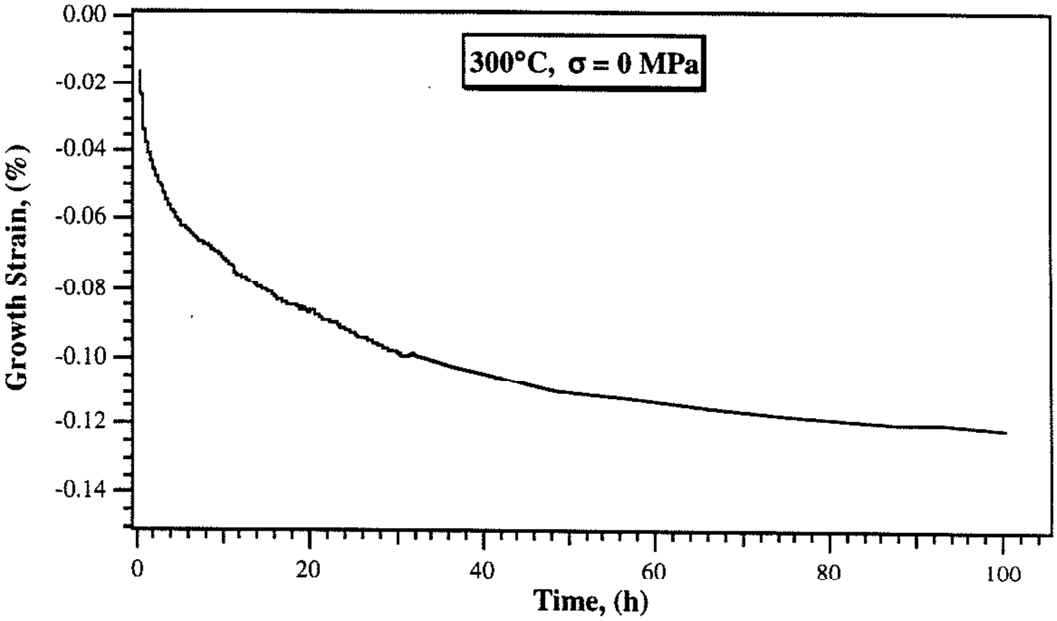

Figure 25: ε^{in} vs. time recorded during a zero-stress thermal exposure test at T=300°C.

Negative creep was not observed in the creep test performed at 250°C, since the rate of decomposition of θ' was decreased and consequently did not cause large volume changes before the sample had already undergone substantial creep deformation. Thus, negative creep is completely masked by rapid tertiary creep at low temperatures. Hence, the presented stress-strain model would not predict a creep curve such as the one shown in Figure 24 as the model is based on creep tests conducted at both 150°C and 250°C.

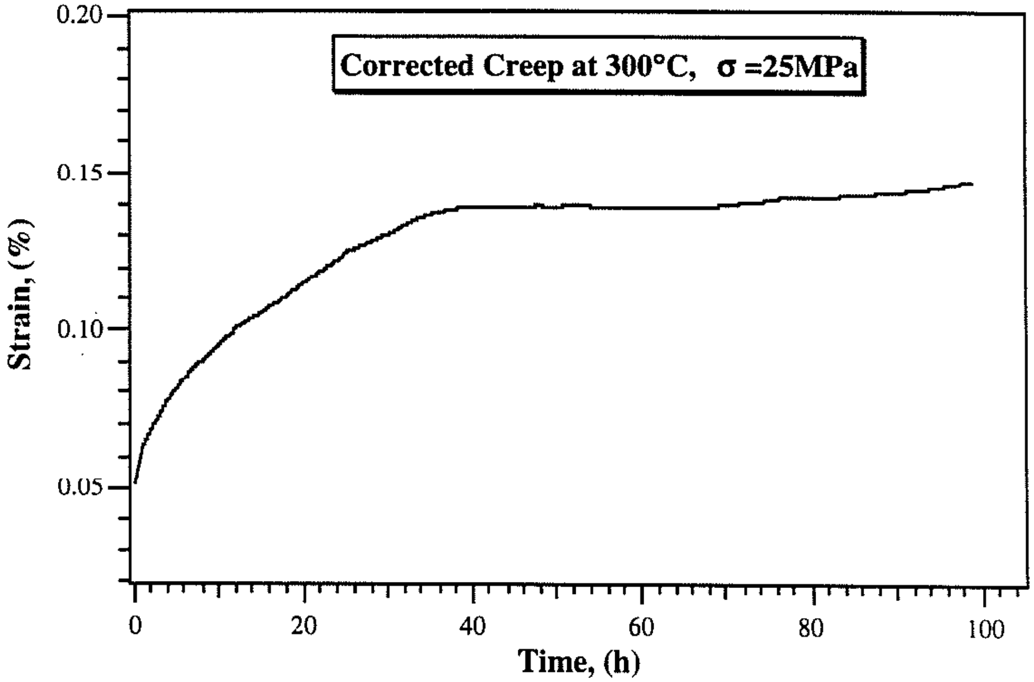

Figure 26: Creep response at 25 MPa and 300°C after correction for thermal-induced contraction. See text for details.

To determine if thermal contraction effects could be incorporated into the model, the temperature-induced inelastic strain obtained from Figure 25 was subtracted from the experimentally obtained creep response shown in Figure 24. Clearly, this approach assumes that the decomposition of θ' prime is not affected by the applied creep stress. However, it has been shown[23,24] that the decomposition process is slower in creep tests as compared to unstressed samples. Thus, it is expected that this simple approach should only give an approximate correction to the creep curve obtained at 25 MPa. As seen in Figure 26, after subtraction of the temperature-induced component the resulting creep curve approximately resembles a conventional creep curve. Note that towards the end of the 100h test period shown, the slope of the modified creep curve now starts to approach the creep rate predicted from the flow rule, as the thermal contraction becomes negligible after 100h, c.f. Figure 25. As far as modeling of the high temperature creep response is concerned, the simple approach used works well in creep tests conducted at high stresses as the thermal contraction becomes negligible. Similarly at extremely low creep stresses the inelastic strain is completely dominated by thermal contraction and the stress-strain response can be accurately predicted using the simple approach of subtracting the thermally induced strains from the experimental results. Thus, only at intermediate stresses as is the case in the test shown in Figure 23, will there be some discrepancy between model prediction and experiment.

7. DISCUSSION

7.1 Microstructural Effects on Modeling the Stress-Strain Behavior

High temperature plasticity in these cast aluminum alloys is controlled largely by the precipitates within the dendrites. Most of the alloying elements are either accumulated within the interdendritic regions or form large phases such as silicon which have a relatively small effect on plastic stress-strain response. Hence, as seen in Figure 4a, the microstructure within the dendrites closely resembles those found in binary aluminum-copper alloys, which have been studied extensively. In the following we will compare the present microstructural observations with studies on Al-4wt.-%Cu and discuss the implications of these observations on modeling of the stress-strain behavior.

As has been demonstrated by Bhat and Laird[25] the cyclic flow stress in aluminum alloys with metastable plate-like θ' precipitates is controlled by the precipitate spacing. It should be noted that the alloy used in the present study also contained finely dispersed θ precipitates, as seen in Figure 4b. Whereas Figure 4b suggests that the latter are uniformly distributed throughout the matrix, close inspection including stereo imaging suggested that most of the fine θ precipitates were associated with the θ' - matrix interfaces. Note also that only two of the three different θ' variants are clearly visible. Thus the apparent uniform distribution of the fine theta is mostly due to a thin foil projection effect and the spacing of the θ' precipitates will still control the cyclic flow stress. The fine θ precipitates result from the over-aged heat treatment used, which was chosen to represent that used in commercial cylinder heads.

In the presented constitutive model, the actual plastic strain rate depends on both the drag stress K and the deviatoric back stress S^c_{ij}. Since the initial value of the drag stress (K_o), was calculated based on yield stress measurements it is governed mainly by the precipitate spacing. Thus K_o, should depend only weakly on temperature, c.f. Figure 14. Using the above argument, the observed softening can be understood based on an increase in the slip distance. In the present study, depending on test conditions, indications of complete decomposition of θ' to θ and coarsening of both θ' and θ were observed. The extreme softening seen after both long-term high-temperature exposure and during cyclic deformation was implemented in the model through the decrease in K via the drag stress recovery and cyclic softening functions. Figure 14 indicates that at 250°C both K_{rec} and K_{sat} approach similar values. If both Figure 15 and Figure 16 are compared to Figure 4 it is obvious that the microstructure has coarsened substantially. An increase in coarsening and/or decomposition rate as a result of high-temperature cyclic deformation has been reported in various studies[21-22]. Decomposition of θ' and subsequent coarsening of θ depend on a diffusion process and it has been argued that an increase in vacancies as a result of cyclic deformation will enhance the diffusion processes and thus enhance cyclic softening. Plastic deformation of θ' is expected during high temperature deformation at large strains[25] and is also visible in Figure 16. This effect should also increase the decomposition of θ'[26]. Our experimental observation that deformation causes accelerated coarsening has been implemented in the model via an increase in the drag stress recovery term whenever $\left(\frac{\bar{\sigma}}{K}\right) > 1.1$, i.e. when deformation occurs in the plasticity regime (see Appendix A). Thus, the model predicts low drag stress recovery rates for unstressed material, as well as for creep deformation. The decomposition of θ' under creep conditions, which is indeed much lower than in the plasticity regime, has been reported for both a pure Al-4Cu alloy[23] and a commercially used aluminum 2219 alloy[24].

Figure 14 demonstrates that cyclic deformation at low temperatures also results in a substantial decrease in K. However, cyclic deformation of Al-4wt.-%Cu alloys at low temperatures is reported to lead to cyclic hardening[27], whereas Figure 14 indicates that cyclic deformation causes a substantial decrease in the drag stress (K_{sat}) even at the lowest temperatures studied. Similarly, the cyclic stress-strain response curves of samples fatigued at room temperature indicated slight initial cyclic hardening followed by cyclic softening. It is assumed that the cyclic softening observed in the present study is caused by the fine θ precipitates already present in the initial stage as no nucleation phase for θ formation is required. Microstructural stability is also affected by other factors such as the secondary dendrite arm spacing

The coarsening of the microstructure also affects the strain hardening behavior. The drastic changes in stress-strain response are demonstrated in Figure 20. Strain hardening in the model is incorporated through the accumulation of a back stress. Microscopically, the back stress can be associated with dislocation pile-ups and statistically stored dislocations at interfaces. Similar to Al-4wt.%Cu alloys[28] dislocation loops around θ', that accommodate the residual misfit between the precipitate and the matrix, were observed in the undeformed material. In deformed samples an overall increase in dislocation density as well as an increase in dislocations statistically stored at interfaces were also observed. These increases cause a back stress which is eventually balanced by recovery processes yielding to steady state deformation as depicted in the tensile tests, c.f. Figure 17. In the case of cyclic deformation, however, the coarsening of the microstructure is the dominating effect and few dislocations are present at the interfaces, see Figure 16. As a result, dislocation-dislocation interactions become more dominant. In the extremely overaged structure seen in Figure 15, the coarse precipitates hardly affect the strain hardening behavior and the stress response is drastically altered, see Figure 19. To account for this effect in the model, the hardening function (h_{α}) was made dependent on exposure time and temperature, see Appendix A.

The examples presented in Chapter 5 demonstrated that the constitutive model accurately captures the effect of strain rate (Figures 18a and b), temperature (Figure 17), thermal exposure (Figure 20) and monotonic and cyclic loading conditions (Figure 17 and Figures 19). As shown, the material constants can be determined directly from the experiments if designed such that the various contributions to deformation can be separated. Moreover, the microstructural studies have shown that the material constants can be related to certain microstructural processes. Thus, it is expected that the model has predictive capabilities and can be used to model deformation behavior even under conditions that were not covered in the experiments used to establish the constants. Chapter 6 proved this assumption by demonstrating that the constitutive model is capable of quite accurately predicting the material behavior over a broad range of loading conditions. It should be noted that the satisfactory prediction of the TMF test with a peak temperature of 300°C is possible without using any monotonic or cyclic tests conducted at 300°C in establishing the model constants. Only one creep test conducted at 300°C was used to establish the flow rule for this temperature. This indicates that the model captures the predominant deformation mechanisms and microstructural changes as a function of temperature and inelastic strain rate.

7.2 The Effect of Solidification Rate on the Material Behavior

As seen in Figure 7 the cyclic stress-strain response is significantly affected by the SDAS, i.e. the initial microstructure. The TEM studies performed thus far have indicated that the faster cyclic softening observed in the material with large SDAS value can be attributed to a more rapid decomposition of θ' and more rapid coarsening of θ, c.f. Figures 8a and b. For a given total strain range, the large SDAS material displayed substantially wider hysteresis loops, i.e. more plastic strain is accumulated within in a cycle. As previously discussed, the decomposition of the θ' precipitates was drastically accelerated by plastic deformation, which explained why the large SDAS material showed significantly faster cyclic softening, c.f. Figure 7.

Various studies[8,5] have clearly demonstrated that the material behavior of cast aluminum-copper-silicon alloys is not only affected by the SDAS value but depends largely on the actual processing history. Factors such as porosity[7], silicon modification[7,29] and intermetallic constituents[8] all effect the material behavior. The SDAS value is often quoted only, as this value is an easily measurable microstructural quantity. However, porosity might be different for similar SDAS values. In general, control of porosity is by far the most important factor and it has been shown[8] that thermal fatigue life under certain test conditions might vary by almost an order of magnitude for material within the Al 319 specification. However, as demonstrated for cast 320 aluminum-silicon[7], metallographically measured pore size distributions did not correlate well with pore size measurements obtained from the fracture surface and consequently the actual cast quality can not be defined by using only a single metallographically obtained parameter, such as porosity percentage.

Similarly, the significant difference in fatigue life between the small SDAS material and that with large SDAS (Figure 7) result not only from porosity. The relatively high porosity content of approx. 1% in the large SDAS material eases crack nucleation. Moreover, SEM studies showed that in the large SDAS material the cracks propagated preferentially within the interdendritic regions tended to avoid the dendrites. Thus, the enhanced fatigue life in the small SDAS material is believed to result, not only from a reduction in the ease of crack nucleation due to the low porosity level of approx. 0.1 % but also from a reduced rate of crack propagation within the much finer microstructure.

Dimensional instabilities caused by high-temperature exposure as seen in Figure 24, might seriously affect an engine's performance. It should be noted, however, that Figure 24 is not easily applicable to a real component such as a cylinder head. Due to the constraints present in a component, thermal contraction will result in the build-up of stresses, which in turn would relax as a result of the high-temperature exposure itself. Also, as previously outlined, the contribution of thermal growth (or contraction) to overall deformation is often less marked at lower temperatures and other contributions such as creep might dominate the material response. Modeling of dimensional changes at high temperature is complicated by the fact that thermal growth also depends on the actual stress. As seen in Figure 23, the stress-strain response at intermediate stresses and high temperatures might be quite different from the expected response under such conditions. However, extremely high temperatures such as those used in the thermal growth studies will only occur during a very short portion of a TMF cycle, or the start-up transient of an actual engine. Thus, the simple approach that assumes stress independent thermal growth should still predict the material behavior quite accurately. Moreover, Figure 24 was obtained from material with a SDAS of approximately 60µm. Similar to the effect of SDAS on microstructural stability during cyclic deformation, it is expected that reducing the SDAS will also have a beneficial effect on thermal growth. As material with smaller SDAS value is more characteristic of the most highly stressed parts in an cylinder head, i.e. the valve bridge area, less thermal growth is expected in that region and the modeling of stress-strain response under actual service conditions should be more accurate. At present, studies on the effect of heat treatment and SDAS on thermal growth are in progress.

Recent work[8] on cast Al 319 and Al 356 alloys has demonstrated that the life under thermal fatigue conditions is more affected by actual casting process than by alloy chemistry. The material used for the present study was machined from a well controlled casting, and the variability observed in the data used to establish the model constants was thus relatively small for a cast material. The large variability in material behavior caused by the solidification conditions requires a stringent control of the casting process if a material model is to be applied successfully to predict the behavior of an actual component.

8. CONCLUSIONS

A unified creep-plasticity constitutive model has been applied to a cast aluminum alloy. The present study was aimed at understanding and modeling the stress-strain behavior of cast aluminum-copper-silicon alloys under complex loading conditions. Microstructural variables affecting the deformation behavior were identified and model predictions of the stress-strain response of the material under a variety of loading conditions were compared to experiments. The results of this work can be summarized as follows:

1. The model allows quite accurate simulation of the experimentally obtained stress-strain behavior over a wide range of deformation conditions. Strain rate sensitivity, cyclic softening and aging effects are all accounted for in the model.

2. Thermo-mechanical fatigue tests and isothermal fatigue tests with dwell periods provided an independent check of the predictive capabilities of the model. The model predicted the stress-strain response in these tests quite satisfactorily.

3. All model parameters can be derived from experiments following a systematic method. In the present study emphasis was on accurate simulation of stress-strain behavior at small plastic strains such as those encountered during service conditions.

4. The microstructural processes affecting the material behavior have been identified and the correlation to the parameters used in the model has been demonstrated. Coarsening of the precipitates results in significant cyclic softening and a substantial decrease in the drag stress subsequent to long-term thermal exposure.

5. The stress-strain behavior is influenced mostly by the decomposition of the metastable θ' precipitates within the dendrites and subsequent coarsening of the θ phase. This process is enhanced significantly during cyclic deformation and was incorporated into the model by allowing for an increase in the drag stress recovery during deformation.

6. Pronounced dimensional instabilities were observed to occur rapidly if the material was exposed to 300°C. At temperatures of 250°C and below this process was already slowed drastically and usually masked in most experiments by other processes such as creep deformation. The thermally-induced dimensional changes can be easily incorporated into the existing model if temperatures and stresses are limited to levels occurring in cylinder heads during actual operating conditions.

7. Cyclic deformation behavior was found to depend significantly on solidification conditions. Rapidly solidified material with small secondary dendrite arm spacing (SDAS) displayed higher cyclic stresses and less plasticity for a given strain range than material with large SDAS.

8. Cyclic softening was also much reduced in the small SDAS material. Transmission electron microscopy revealed that softening is caused by the decomposition of the θ' precipitates. As plastic deformation was found to enhance the decomposition rate of the precipitates, the initially softer large SDAS also exhibited faster cyclic softening.

REFERENCES

1. D.Slavik and H. Sehitoglu, "A Constitutive Model for High Temperature Loading Part 1--Experimentally Based Forms of the Equations," *ASME PVP 123*, 1987, pp. 65-73.
2. J.B. Heywood: *Internal Combustion Engine Fundamentals*, McGraw-Hill Publishing Corp., New York, NY, 1988, pp. 699.
3. J.A. Allison: Ford Motor Company, Scientific Research Laboratory, Dearborn, MI, private communication, 1997.
4. R. Chuimert and M. Garat, "Aluminum Casting Alloys for Highly Stressed Diesel Cylinder Heads," *3rd International Symposium Aluminum and Automobile*, Dusseldorf, Germany, 1988, pp.154-159.
5. A. Wickberg, G. Gustafson, and L.E. Larson,. "Microstructural Effects on the Fatigue Properties of a Cast A17SiMg Alloy," *SAE Transactions*, 1984, vol. 93, pp. 728-735.
6. O. Vorren, J.E. Evensen, T.B. Pedersen, "Microstructure and Mechanical Properties of AlSi(Mg) Casting Alloys", *AFS Transactions*, 1984, vol. 92, pp.459-466.
7. J.M. Boileau and J.E. Allison, "The Fatigue Behavior of a Cast 320 Aluminum Alloy," *Fatigue '96*, Proc. 6th Int. Fatigue Congress, Berlin, Germany, 1996, pp. 941-946.
8. R.B. Gundlach, B. Ross, A. Hetke, S. Valtierra, and J.F. Mojica, "Thermal Fatigue Resistance of Hypoeutectic Aluminum-Silicon Casting Alloys," *AFS Transactions*, 1994, vol. 102, pp. 205-223.
9. H. Beumler, A. Hammerstad, B. Wieting, and R. DasGupta, "Analysis of a Modified 319 Aluminum Alloy," *AFS Transactions*, 1988, vol. 96, pp. 1-12.
10. R. Vijayaraghavan, N. Palle, J. Boileau, J. Zindel, R. Beals, and F. Bradley, "Micro-model for Aluminum-Silicon Alloys," *Scripta Mater.*, 1996, vol. 35, pp. 861-867.
11. H.R. Shercliff and M.F. Ashby, "A Process Model for Age Hardening of Aluminum Alloys--I. The Model," *Acta Metall. Mater.*, 1990, vol. 38, pp. 1789-1802.

12. J.A. Eady and D.M. Smith, "Properties and Applications of a New Aluminum Foundry Alloy," *SAE Transactions*, 1984, vol. 93, pp. 747-755.

13. G.K. Sigworth, "Theoretical and Practical Aspects of the Modification of Al-Si Alloys." *AFS Transactions*, 1983, vol. 91, pp. 7-16.

14. S. Tohriyama and M. Kumano, "Influence of Material and Mechanical Properties on Thermal Fatigue Life of Aluminum Castings," *Aluminum Applications for Automotive Design*, SAE, Warrendale, PA, 1995, pp.47-57.

15. P. Jonason, "Thermal Fatigue of Cylinder Head Alloys," *AFS Transactions*, 1992, vol. 100, pp. 601-607.

16. E. Velasco, R. Colás, S. Valtierra, and J.F. Mojica, "A Model for Thermal Fatigue in an Aluminum Casting Alloy," *Int. J. Fatigue*, 1995, vol. 17, pp. 399-406.

17. J.B. Andrews and M.V.C. Seneviratne, "A New, Highly Wear-Resistant Aluminum-Silicon Casting Alloy for Automotive Engine Block Applications," *AFS Transactions*, 1984, vol. 92, pp. 209-216.

18. A. Hetke and R.B. Gundlach, "Aluminum Casting Quality in Alloy 356 Engine Components," *AFS Transactions*, 1994, vol. 102, pp. 367-380.

19. M.C. Flemings, T.Z. Kattamis, and B.P. Bardes, "Dendrite Arm Spacing in Aluminum Alloys," *AFS Transactions*, 1991, vol. 99, pp. 501-506.

20. R.I. Stevens, H.D. Berns, R.A. Chernekoff, R.L. Indig, S.K. Koh, D.J. Lingenfelser, M.R. Mitchell, R.A. Testin, C.C. Wigant, "Low Cycle Fatigue of A356-T6 Cast Aluminum Alloy - A Round-Robin Test Program," *SAE Technical Paper No. 881701*, 1988.

21. H.J. Frost and M.F. Ashby: *Deformation-Mechanism Maps*, 1st ed., Pergamon, Elmsford, NY, 1982, pp. 1-5.

22. D.C. Stouffer and L.T. Dame: *Inelastic Deformation of Metals*, John Wiley & Sons Inc., New York, NY, 1996, pp. 33-34.

23. V.B. Nileshwar, "Some Observations on the Kinetics of Ageing Reactions during Creep of Aluminium Alloys," *J. Inst. Metals*, 1963-64, vol. 92, pp. 241-245.

24. P.E. Krajewski, J.W. Jones, and J.E. Allison, "The Influence of Matrix Microstructure and Particle Reinforcement on the Creep Behavior of 2219 Aluminum," *Metall. Trans. A*, 1993, vol. 24A, pp. 2731-2742.

25. S.P. Bhat and C. Laird, "High Temperature Cyclic Deformation of Precipitation Hardened Alloy - I. Partially Coherent Precipitates," *Acta metall.*, 1979, vol. 27, pp. 1861-1871.

26. G.M. Vyletel, D.C. Van Aken, and J.E. Allison, "The Effect of Matrix Microstructure on Cyclic Response and Fatigue Behavior of Particle-Reinforced 2219 Aluminum: Part II. Behavior at 150°C," *Metall. Mater. Trans. A* , 1995, vol. 26A, pp. 3155-3162.

27. C. Calabrese and C. Laird, "Cyclic Stress-Strain Response of Two-Phase Alloys Part II. Particles Not Penetrated by Dislocations," *Mater. Sci. Engng.*, 1974, vol. 13, pp. 159-174.

28. W.M. Stobbs and G.R. Purdy, The Elastic Accomodation of Semicoherent θ' in Al-4 wt.% Cu Alloy," *Acta metall.,* 1978, vol. 26, pp. 1069-1081.

29. J.E. Gruzleski and B.M. Closset: *The Treatment of Liquid Aluminum Silicon Alloys*, American Foundrymen's Society, Des Plaines, IL, 1990.

APPENDIX A - EQUATIONS USED IN MODEL DEVELOPMENT

FLOW RULE

Rate Equation

$$\dot{\varepsilon}^{in}_{ij} = \frac{3}{2}\Lambda f\left(\frac{\bar{\sigma}}{K}\right)\frac{S_{ij}-S^c_{ij}}{\bar{\sigma}}$$

Flow Function

$$f\left(\frac{\bar{\sigma}}{K}\right) = \left(\frac{\bar{\sigma}}{K}\right)^{n_1} \qquad \text{when } \left(\frac{\bar{\sigma}}{K}\right) < 1.0$$

$$f\left(\frac{\bar{\sigma}}{K}\right) = \exp\left[\left(\frac{\bar{\sigma}}{K}\right)^{n_2} - 1\right] \qquad \text{when } \left(\frac{\bar{\sigma}}{K}\right) \geq 1.0$$

BACK STRESS EVOLUTION

Rate Equation

$$\dot{S}^c_{ij} = \frac{2}{3}h_\alpha\dot{\varepsilon}^{in}_{ij} - \left[r^D_\alpha\left(\dot{\bar{\varepsilon}}^{in}_{ij}\right) + r^S_\alpha\right]S^c_{ij}$$

Back Stress Hardening

$$h_\alpha = a_1\exp\left[-\left(a_2(\alpha_0+\bar{\alpha})\right)^{a_3}\right] \qquad \text{when } \dot{\varepsilon}^{in}_{ij}.\ S^c_{ij} > 0$$

$$h_\alpha = a_1\exp\left[-\left(a_2(\alpha_0-\bar{\alpha})\right)^{a_3}\right] \qquad \text{when } \dot{\varepsilon}^{in}_{ij}.\ S^c_{ij} \leq 0$$

$$a_1\text{=constant}, \quad a_2 = A'_{2_i}\exp\left[-\frac{\Delta H}{RT}\right], \qquad a_3 = A'_{3_i}\exp\left[-\frac{\Delta H}{RT}\right]$$

where

$$A'_{2_{i+1}} = A'_{2_i} + \left(A'_{2_i} - a_{2_{sat}}\right)a_2\Delta t$$

$$A'_{3_{i+1}} = A'_{3_i} + \left(A'_{3_i} - a_{3_{sat}}\right)a_3\Delta t$$

$a_{2_{sat}}$ =const. and $a_{3_{sat}}$ =const.

Back Stress Recovery

$$r_\alpha^S = 0$$

$$r_\alpha^D = c(\overline{\alpha})^d\left(\dot{\overline{\varepsilon}}^{in}\right)^e$$

$$c = c'\exp\left[-\frac{\Delta H}{RT}\right], \qquad \text{d=const. and e=const.}$$

DRAG STRESS EVOLUTION

Rate Equation

$$\dot{K} = h_k - r_k + \Theta\dot{T}$$

Drag Stress Hardening

$$h_k = B(K_{sat} - K)\dot{\overline{\varepsilon}}^{in}$$

B=const.

Drag Stress Recovery

$$r_k = B_3(K - K_{rec})$$

$$B_3 = B_3'\exp\left[-\frac{\Delta H_r}{RT}\right] \qquad \text{when } \left(\frac{\overline{\sigma}}{K}\right) > 1.1$$

$$B_3 = B_3''\exp\left[-\frac{\Delta H_r}{RT}\right] \qquad \text{when } \left(\frac{\overline{\sigma}}{K}\right) \leq 1.1$$

where $B_3' > B_3''$ and $B_3'' = B_3'$-const.

Drag Stress Temperature Dependence Term

$$\Theta = \frac{\partial K_o}{\partial T}$$

APPENDIX B - MATERIAL CONSTANTS AND PARAMETERS

FLOW RULE

Rate Equation

$$A = 4.05\text{x}10^{12}\exp\left[-\frac{2.14\text{x}10^{5}}{RT}\right]\ (\text{s}^{-1})$$

where R = 8.3143 J/ mol.K and T = temperature in K

Flow Function

$n_1 = 4.9$
$n_2 = 18.6$

BACK STRESS EVOLUTION

Back Stress Hardening

$\alpha_o = 120$ MPa

$a_1 = 4.5\text{x}10^{5}$
$$a_2 = -1.522\text{x}10^{4}\exp\left[-\frac{1.0\text{x}10^{5}}{RT}\right]$$
$$a_3 = -5.15\text{x}10^{3}\exp\left[-\frac{8.8\text{x}10^{4}}{RT}\right]$$

$A'_{2_{(i=1)}} = 0.0083$
$A'_{3_{(i=1)}} = 1.80$

$a_{2_{sat}} = 0.034$
$a_{3_{sat}} = 0.82$

Back Stress Recovery

$$c = 1.7\text{x}10^{6}\exp\left[-\frac{3.3\text{x}10^{4}}{RT}\right]$$

where R and T are defined above.

$d = -0.5$

$e = -0.25$

DRAG STRESS EVOLUTION

Drag Stress Hardening

$B = 2.0186$ MPa/s

Drag Stress Recovery

$B_3 = 4.61\text{x}10^{-7}$ MPa/s when $\left(\frac{\overline{\sigma}}{K}\right) > 1.1$

$B_3 = 2.31\text{x}10^{-5}$ MPa/s when $\left(\frac{\overline{\sigma}}{K}\right) \leq 1.1$

Drag Stress Temperature Dependence

$\Theta = -3.02\text{x}10^{-2}$ MPa/K

ADDITIONAL MATERIAL PARAMETERS

Coefficient of Thermal Expansion	$\alpha_e = 2.15\text{x}10^{-5}$ (°C^{-1})	
Young's Modulus	$E = 7.4\text{x}10^{4} - 24.1*T$ (MPa)	T in °C
Saturated Drag Stress	$K_{sat} = 37.64 - 0.0422*T$ (MPa)	T in °C
Recovered Drag Stress	$K_{rec} = 64.89 - 0.145*T$ (MPa)	T in °C
Initial Drag Stress	$K_o = 64.56 - 0.030*T$ (Mpa)	T in °C